An Observational Verification of the
Arakawa-Schubert Cumulus Parameterization

by

S. Lord

UNIVERSITY OF CALIFORNIA, LOS ANGELES, U S A

The purpose of this paper is to present some results of a verification of the Arakawa-Schubert cumulus parameterization obtained by applying it to observed data. After a brief review of the parameterization, some supporting evidence for the closure assumption, the cloud work function quasi-equilibrium, is presented. Then the entire parameterization is evaluated by comparing the precipitation rates and the cumulus warming and drying predicted by the parameterization with observed estimates over the same time period during Phase III of GATE.

In the Arakawa-Schubert cumulus parameterization, we consider a horizontal slice at height z through the atmosphere as shown in Fig. 1. The unit horizontal area is large enough to contain an ensemble of many cumulus clouds in different stages of their life cycles but covers only a small fraction of a large-scale disturbance. It is also assumed that the fractional area covered by active cumulus convection, σ, is small. Environmental air is mixed into clouds penetrating this level during their growth and mature stages and cloud air is mixed back into the environment by clouds in their mature and decaying stages. The downward mass flux in the environment is $M_c - \rho\overline{w}$ where M_c is the total ensemble cloud mass flux penetrating this unit area, $\rho\overline{w}$ is the large-scale net vertical mass flux and the overbar ($\overline{}$) indicates a large-scale area average.

The budget equations for dry static energy (s) and water vapor mixing ration (q_v) averaged over this hypothetical area may be written as

$$\rho \frac{\partial \overline{s}}{\partial t} = \hat{D}[(\hat{s} - L\hat{q}_\ell) - \overline{s}] + \sum_{i'} D_{i'}[(s - Lq_\ell)_{i'} - \overline{s}] + M_c \frac{\partial \overline{s}}{\partial z} \qquad (1)$$

$$-\rho \overline{\mathbf{V} \cdot s} - \rho\overline{w} \frac{\partial \overline{s}}{\partial z} + \overline{Q}_R$$

and

$$\rho \frac{\partial \overline{q}_v}{\partial t} = \underline{\hat{D}}[\hat{q}_v^* + \hat{q}_\ell - \overline{q}_v] + \sum_{i'} \underline{D}_{i'} \cdot [(q_v + q_\ell)_{i'} - \overline{q}_v] + \underline{M}_c \frac{\partial \overline{q}_v}{\partial z} \qquad (2)$$

$$- \rho \, \overline{\mathbb{V} \cdot \nabla q}_v - \rho \overline{w} \frac{\partial \overline{q}_v}{\partial z} \, ,$$

where $\overline{Q}_R = \tilde{Q}_R + \sum_i \hat{Q_{Ri}}$ is the radiational heating per unit height over the large-scale area and depends on contributions from both the large-scale environment, $\tilde{Q}_R$, and the clouds, $\hat{Q_{Ri}}$,[1] $\hat{D}$ and $D_{i'}$, are respectively the mass detrainment from clouds at their top levels and from the lateral edges of clouds, and q_ℓ the cloud suspended liquid water droplet mixing ratio. The summation $\sum_{i'}$ is over all clouds penetrating height z, $\overline{\mathbb{V} \cdot \nabla}$ represents the horizontal advection of s or q_v and $(\ )^*$ denotes a saturation value.

The budget equations (1) and (2) show explicitly the feedback of cumulus convection on the large-scale thermodynamical fields. The first two terms on the right-hand side (r.h.s.) of (1) represent the changes due to detrainment of cloud air at a different temperature from the environment and to evaporation of detrained suspended liquid water droplets. The third term gives the warming (since $\frac{\partial \overline{s}}{\partial z} > 0$) due to subsidence between clouds. The first two terms of on the r.h of (2) represent the moistening due to detrainment of saturated cloud air containing liquid water and the third term gives the drying (since $\frac{\partial \overline{q}_v}{\partial z} < 0$ in most cases) due to the subsidence.[2]

The interaction of a cumulus ensemble with the large-scale radiation fields has not been completely solved. If the dependence of $\overline{Q}_R$ on cumulus clouds is known, then only the underlined quantities in (1) and (2) namely, $\hat{D}$, $\hat{s}$, $\hat{q}_\ell$, $D_{i'}$, $s_{i'}$, $(q_\ell)_i$, $\hat{q}_v^*$, $(q_v)_i$, and M_c, are unknown functions of the

---

[1] $(\hat{\ })$ denotes a cloud top value.

[2] The interaction of cumulus clouds with the subcloud layer will not be treated in this paper. This topic is discussed by Arakawa and Schubert (1974), Lord (1978) and Randall (1976).

cumulus activity within the large-scale area. To solve the parameterization problem, we must determine them in terms of the large-scale variables, $\bar{s}$, $\bar{q}_v$, $\bar{V}$ and $\bar{w}$. From (1) and (2) we see that it is then possible to predict the large-scale temperature and moisture fields from the large-scale variables.

Arakawa and Schubert (1974) have shown that if the individual cumulus clouds in the ensemble are spectrally classified into sub-ensembles, $\hat{D}$ can be calculated from the spectral distribution of mass flux into each sub-ensemble. Likewise D_i, can be calculated from the mass budget of each sub-ensemble when the detrainment of mass from individual clouds has been formulated. The sub-ensemble thermodynamical properties can be found from the sub-ensemble moist static energy and total water budgets when a parameterization of the cloud microphysical processes is given. The cloud ensemble model used in this work is very similar to that presented by Arakawa and Schubert (1974). As shown schematically in Fig. 2, entrainment is allowed at each level, k, penetrated by the cloud (including the cloud top level, i), and detrainment from the lateral edges of the clouds is also allowed at all levels. Details of the cloud ensemble model are given in Lord (1978). If it is assumed that the cloud top occurs at a level of non-buoyancy for the cloud air, this model reduces the parameterization problem to the determination of the amount of mass distributed into the ith sub-ensemble at cloud base, $m_B(i)$. $m_B(i)$ is known as the mass flux distribution function.

To determine the mass flux distribution function we need to apply a closure assumption about the statistical behavior of cumulus clouds. The physical basis for the closure assumption used in the Arakawa-Schubert cumulus parameterization is diagrammed in Fig. 3. Cumulus cloud-scale kinetic energy is the manifestation of a moist convective instability in the large-scale

environment. The large-scale budget equations (1) and (2) show that cumulus mass flux induces environmental subsidence and produces a stabilization of the lapse rate and drying of the large-scale environment, thereby reducing the moist convective instability. On the other hand, the large-scale processes, consisting of horizontal and vertical advections of the thermodynamical variables, surface fluxes of heat and moisture and radiational cooling, tend to destabilize the lapse rate and moisten the environment. These processes generate moist convective instability and therefore generate cloud-scale kinetic energy. The closure assumption of the Arakawa-Schubert parameterization expresses the approximate balance between the processes generating and reducing the moist convective instability.

Since the primary source of kinetic energy generation for penetrative cumulus convection is the buoyancy force, Arakawa and Schubert defined the cloud work function, $A(\lambda)$, as an integrated measure of the sub-ensemble kinetic energy generation by the buoyancy force per unit of mass flux at cloud base,

$$A(\lambda) = g \int_{z_B}^{\hat{z}(\lambda)} \frac{\eta(z,\lambda)}{\overline{T}} [(T_v)_c - \overline{T}_v] \, dz, \qquad (3)$$

where λ is a parameter which characterizes the sub-ensemble, $\eta(z,\lambda)$ is the sub-ensemble mass flux normalized at cloud base,

$$M_c(z,\lambda) = \mathcal{M}_B(\lambda) \, \eta(z,\lambda), \qquad (4)$$

$(T_v)_c$ and $\overline{T}_v$ are respectively the sub-ensemble and large-scale virtual temperatures, and z_B and $\hat{z}(\lambda)$ are the heights of cloud base and cloud top. Arakawa and Schubert have also shown that $A(\lambda)$ is a generalized measure of

the moist convective instability in the large-scale environment.

We now examine the modification of the cloud work function by both the cumulus and large-scale processes by writing the total change of as

$$\frac{dA}{dt} = [\frac{dA(\lambda)}{dt}]_{LS} + [\frac{dA(\lambda)}{dt}]_{CU}, \tag{5}$$

where the subscripts "LS" and "CU" refer to large-scale and cumulus processes respectively. From Eqs. (1), (2) and (4) we see that the cumulus feedback on the large-scale thermodynamical fields is a linear function of $\eta_B(\lambda)$. Therefore, for each sub-ensemble, we can write the cumulus effects as an integral over all existing cloud types of the product of $\eta_B(\lambda)$ and a kernel, $K(\lambda,\lambda')$,

$$[\frac{dA(\lambda)}{dt}]_{CU} = \int_0^{\lambda_{max}} K(\lambda,\lambda')\eta_B(\lambda')d\lambda'. \tag{6}$$

The kernel therefore represents the amount of stabilization of type λ cloud per unit cloud base mass flux of type λ' cloud. The form of $K(\lambda,\lambda')$ has been derived by Arakawa and Schubert (1974) for their cloud model and the mutual influence between different sub-ensembles described by the kernel is discussed in that paper. A numerical method for calculating $K(\lambda,\lambda')$ is described in Lord (1978).

We may also equate $(\frac{dA(\lambda)}{dt})_{LS}$ in Eq. (5) to the large-scale forcing, $F(\lambda)$, defined by A-S,

$$[\frac{dA(\lambda)}{dt}]_{LS} = F(\lambda). \tag{7}$$

$F(\lambda) > 0$ indicates growth of the cloud work function due to large-scale processes, i.e. destabilization of the cumulus clouds. In practice, it

is not necessary to compute the analytical forms of $F(\lambda)$ as given by Arakawa and Schubert. A simpler numerical procedure is described in Lord (1978).

Substituting (6) and (7) into (5) we have

$$\frac{dA(\lambda)}{dt} = \int_0^{\lambda_{max}} K(\lambda,\lambda')\mathfrak{M}_B(\lambda')d\lambda' + F(\lambda). \tag{8}$$

The closure assumption for this parameterization is that the destabilization of clouds by the large-scale processes is approximately balanced by the cumulus self-stabilization. This balance is expressed by setting the left-hand side (l.h.s.) of (8) equal to zero. It is quite clear that

$$\frac{dA(\lambda)}{dt} << F(\lambda) \tag{9}$$

is necessary for closure. Arakawa and Schubert (1974) provided some evidence for this statement using data from the Marshall Islands. We now present similar evidence from the GATE and other data sets from widely varying synoptic conditions in the tropics and sub-tropics.

Fig. 4 is a time series of the large-scale cloud layer forcing from GATE Phase III B and A/B-scale data. The data were provided by Professor R. Reed of the University of Washington and are described in Thompson et al 1978. The data processing procedure is also discussed in Thompson et al and Lord (1978). The abscissa is time, from 1-18 September, and the ordinate is the cloud top pressure, $\hat{p}$, for each sub-ensemble.[1] Contour lines indicate equal values of the large-scale forcing in units of kj $kg^{-1}day^{-1}$. Note the maxima

---

[1]Henceforth, we will use the cloud top pressure as the parameter which characterizes the sub-ensemble.

in forcing on September 2,4,9, 13 and 16 corresponding to the large-scale easterly waves passing over the GATE array.

Fig. 5 is a time series of the observed time change of the cloud work function for each sub-ensemble from the same data. The contour lines are identical to the previous figure and the dashed line indicates the zero line. We note that $\frac{dA}{dt}/F \ll 1$ during disturbed conditions for virtually all cloud types. Although $\frac{dA}{dt}$ is often the same magnitude as the large-scale forcing when the forcing is small, the cumulus activity under these conditions is very weak. Therefore, neglecting the left-hand side (l.h.s.) of (8) is not likely to results in large errors in the estimation of cumulus effects.

We have also calculated the cloud work function from vertical distributions of temperature and moisture at the locations shown in Fig. 6. The AMTEX was held in two separate two-week periods in February of 1974 and 1975. The tropical cyclone and hurricane data are composited with respect to the center of the disturbance from 10 years of data in the West Pacific and 14 years in the West Indies. The Marshall Islands data has been discussed by Yanai et al (1973). The VIMHEX data were taken in 1972 and Jordan's (1958) mean West Indies sounding was taken from 10 years of data. The GATE data are the same as described above. These data represent a wide variety of synoptic conditions since both undisturbed and highly disturbed conditions are included.

Mean values of the cloud work function for each cloud type for the Marshall Islands, VIMHEX, GATE and AMTEX data sets are shown in Fig. 7. Error bars represent one standard deviation from the mean. We see that the mean cloud work functions from the Marshall Islands lie within the error bars for the GATE for all cloud types. The mean values for AMTEX, although derived from only a few cases, are very close to the GATE mean values. The mean cloud

work functions for VIMHEX are consistently higher than the means for other data sets and the standard deviations are much larger. Even so, the error bars for VIMHEX encompass the mean values for each of the other areas.

Figure 8 shows that there is virtually no difference between the "disturbed" and "undisturbed" cases[1] for the Marshall Islands data except for the deepest 150 mb clouds that show somewhat different standard deviations. The cloud work functions for Jordan's sounding are very close to the Marshall Islands averages for clouds with tops below 250 mb. The tropical cyclone composite cloud work functions increase consistently toward the disturbance center but are nevertheless confined within the narrow ranges defined by other data. The values for Radius R = 2^O and R = 4° latitude from the disturbance center lie very close to the mean values of at least one of the other data sets and within the error bars of all other data sets. The R = 0.7^O values are consistently larger for clouds with tops between 300 and 600 mb but lie within the error bars for GATE.

The West Indies hurricane composite results shown in Fig. 9 give values of A centered at R = 2^O, 4° and 6°. As in the tropical cyclone cases, regions closer to the hurricane center show generally higher values of A. The agreement between the two composite data sets is very good for each radius. Again, the hurricane results are very close to the GATE mean values for most cloud types.

The small differences between the cloud work functions for a particular sub-ensemble are interpreted as evidence for the strong coupling between the temperature and moisture fields throughout most of the troposphere. This coupling

---

[1]Classification into disturbed and undisturbed cases followed the method of Yanai et al (1976).

can only result from the influence of cumulus convection. Arakawa and Schubert (1974) have shown that A can be written as[1]

$$A(\lambda) = \int_{z_B}^{\hat{z}(\lambda)} \rho(z)\beta(z) \left\{ h_M - \bar{h}^*(z_{B+}) + \int_{z_{B+}}^{z} \left[\lambda L(\bar{q}_v(z') - \bar{q}_v^*(z')) - \frac{\partial \bar{h}^*}{\partial z'} \right] dz' \right\} dz \quad (9)$$

where

$$\rho(z)\beta(z) = \frac{g}{c_p \bar{T}(z)[1+\gamma(z)]} .$$

The $\frac{\partial \bar{h}^*}{\partial z'}$ term in the square brackets can be written as $c_p[1+\gamma(z')](\bar{\Gamma}-\bar{\Gamma}_m)$ where $\bar{\Gamma}$ is the lapse rate in the environment and $\bar{\Gamma}_m$ is the lapse rate along a moist adiabat. Therefore, A is composed of the buoyancy at cloud base, $h_m - \bar{h}^*(z_{B+})$, and a double integral over the cloud height of a quantity $\bar{B}(z')$ composed of two opposing terms:

$$\bar{B}(z') = c_p[1+\gamma(z')][\bar{\Gamma}-\bar{\Gamma}_m] - \lambda L[\bar{q}_v^*(z') - \bar{q}_v(z')] . \quad (11)$$

The first term of $\bar{B}(z')$ is proportional to $\Gamma-\Gamma_m$ and is ~~therefore~~ 1) proportional to the conditional instability in the large-scale environment and 2) positive in regions of convection. The second term is proportional to the relative humidity and is generally non-positive over a large-scale area. Therefore, the fact that the cloud work function is a quasi-constant for each cloud type implies that a relatively dry atmosphere has larger lapse rate than a more moist atmosphere. Figs. 10 and 11 which show temperature and relative humidity versus height for Jordan's sounding and the tropical cyclone soundings support this interpretation. Jordan's sounding had the largest lapse rate and also had the lowest relative humidity at each level; the relative humidity was highest and the air was most stable near the center of the tropical cyclone. We also note that differences

---

[1]Virtual temperature effects are ignored.

in relative humidity between each of these soundings were about 10 percent. These differences are sufficient to produce very large changes in A for a given temperature profile as seen in Fig. 12.

Figure 12 shows the cloud work functions calculated using the observed temperature profile for the $R = 2^{O}$ tropical cyclone case but with the relative humidities artificially modified by 5 percent increments. We see that A changes significantly for all cloud types. In fact, a change of $\pm$ 5 percent in relative humidity is sufficient to place the cloud work functions well outside the typical ranges for each cloud type shown in Figs. 7-9. Similar results have been obtained by fixing the observed moisture profile and artificially changing the temperature lapse rate.

We may estimate the order of magnitude of the $\frac{dA}{dt}$ term in Eq. (8) by considering the typical variations of A, δA, as shown in Figs. 7-9. For example, let us assume that the change of A from Jordan's mean West Indies sounding to $R = 2^{O}$ in the hurricane takes place over a period $\tau = 1$ day. For 350 mb clouds, we estimate $\frac{dA}{dt} \sim \frac{\delta A}{\tau} = 0.14$ kj kg^{-1} day^{-1}. There are presently no estimates of the large scale forcing, $F(\lambda)$, for hurricanes, but Arakawa and Schubert (1974) have shown forcings of approximately 4 kj kg^{-1} day^{-1} from the Marshall Islands and Fig. 4 shows similar magnitudes for 350 mb clouds during disturbed conditions over the GATE area. These are clearly conservative estimates of the forcing in hurricanes but they still illustrate that Eq. (8) holds to a good approximation. Similar arguments can be made for other data sets if we take the standard deviation as a measure of the variation of A over a large-scale area and again use 1 day as the relevant time scale for the change of A.

These results should be regarded as an initial step in the verification of the Arakawa-Schubert parameterization. However, without taking into account

the large-scale processes in the atmosphere that are responsible for generating and maintaining the convection, we cannot measure the success of this parameterization in terms of its ultimate purposes, namely predicting large-scale averaged rainfall rates and cumulus warming and drying effects. Let us briefly consider how observed estimates of the large-scale processes, e.g. advections of thermodynamical quantities, surface fluxes, and radiational heating (or cooling) rates, may be used to study the large-scale effects of cumulus convection, see Fig. 13.

A purely diagnostic study, for example Nitta (1972), combines observed estimates of the large-scale processes with the observed tendencies, $\frac{\partial \overline{T}}{\partial t}$ and $\frac{\partial \overline{q}_v}{\partial t}$, to produce residuals in the large-scale budgets. The residuals, customarily referred to as the observed heat source (Q_1) and moisture sink (Q_2) due to subgrid scale activity, are defined by

$$Q_1 \equiv \frac{\partial \overline{s}}{\partial t} + \overline{\nabla \cdot s V} + \frac{\partial \overline{s w}}{\partial p} \tag{12}$$

and

$$Q_2 \equiv - L \left[\frac{\partial \overline{q}_v}{\partial t} + \overline{\nabla \cdot q_v V} + \frac{\partial \overline{q}_v \overline{w}}{\partial p} \right] . \tag{13}$$

From these residuals and the surface fluxes, we can infer the total amount of precipitation from a vertical column of the atmosphere and, assuming that cumulus clouds are primarily responsible for the subgrid scale vertical transports, we can determine the cumulus warming and drying that satisfy the observed heat and moisture budgets at each pressure level. If we assume a hypothetical cloud ensemble model as, for example, in Yanai et al. (1973), Ogura and Cho (1973), Nitta (1975) and many others, we may derive information about the mass flux of the cumulus clouds imbedded within the large-scale area. A bulk model, e.g. Yanai et al (1973), determines the cumulus mass flux as a function of

height, $M_c(z)$, while the additional assumption of a spectral model yields the distribution of cloud base mass flux as shown by Ogura and Cho (1973), Nitta (1975) and Yanai et al (1976).

Purely diagnostic studies are particularly valuable in describing the gross properties of the cumulus convective transports and vertical distribution of latent heat release. However, the quantities we must predict using a cumulus parameterization are already given from observations and therefore this type of diagnostic study cannot verify a cumulus parameterization.

The method used in this study utilizes observed estimates of the large-scale processes to determine the forcing of a cumulus ensemble at a given time. A cumulus ensemble model combined with a closure hypothesis together form a parameterization describing the interaction of the cumulus ensemble with the observed large-scale forcing, again see Fig. 13. In the Arakawa-Schubert parameterization, the cloud mass flux spectrum is predicted using estimates of the large-scale processes and the vertical thermodynamical structure. From the distribution of cloud base mass flux, we may calculate instantaneous values of the precipitation rate and the large-scale warming and drying due to the clouds at each observation time. These values can be compared to observed estimates of the time-and space-averaged precipitation rate and the observed Q_1 and Q_2.

The data used in the following discussions were taken from the processed GATE Phase III B and A/B Scale ship rawinsonde observations provided by Professor Reed as mentioned earlier. The ship arrays during Phase III are shown in Fig. 14. The procedure for obtaining the cloud mass flux spectrum may be found in Lord (1978).

Fig. 15 shows a time series of precipitation rates in units of mm day^{-1} from 1 September to 18 September estimated by the Arakawa-Schubert parameterization,

the observed moisture budget, and observed radar measurements. The estimate

from the observed moisture budget, P_{Q_2}, was computed from

$$P_{Q2} = \int_{100}^{p_s} \frac{Q_2}{L} \frac{dp}{g} + F(\overline{q}_v)_s \qquad (14)$$

where p_s is the surface pressure, Q_2 is given at 3 hourly intervals by the

observations and $F(\overline{q}_v)_s$ is an estimated surface evaporation rate. $F(\overline{q}_v)_s$

was computed using the method of Randall (1976) which used the transfer

coefficients of Deardorff (1972). Surface winds were also taken from the

observed shipboard data. The average evaporation rate over the period shown

was 3.80 mm day^{-1}.

The precipitation rates derived from radar estimates, P_{RA}, are shown

every six hours and were taken from hourly rainfall data over $1/4^o$ x $1/4^o$

latitude-longitude squares computed by Hudlow (1977). Hudlow's data were

processed in the following manner. First, the rainfall over a 12 hour

period centered at a given time was determined from the hourly data and

converted to an average precipitation rate at six hour intervals. Second,

these precipitation rates were time-smoothed by a 1-2-1 weighted average

to bring them into closer agreement with the values of P_{Q2}. This time-

averaging does not, of course, alter the time-averaged precipitation rate.

The time-averaged precipitation rates over this period were $\tilde{P}_{Q2}$ = 14.3 mm day^{-1}

and $\tilde{P}_{RA}$ = 12.4 mm day^{-1}, where ($\tilde{}$) represents a time average over the 18

day period. These estimates differ by about 13 percent.

The instantaneous predicted precipitation rates, P_{AS}, shown in Fig. 15

were calculated from the cloud mass flux spectrum determined by Eq. (8).

Values of $\frac{dA}{dt}$ were taken from the observations shown in Fig. 5. The values of

P_{AS} for each observation time agree closely in both magnitude and phase with the two independently derived observed estimates, P_{Q2} and P_{RA}. $\tilde{P}_{AS}$ in this case was 12.3 mm day^{-1}. There are six peaks in the precipitation rates over the 18 day period which correspond to the six maxima in the forcing field shown in Fig. 4. The values of the maximum P_{AS} occurring at 12/12,[1] and 13/21 are within 10 percent of each of the peaks in P_{Q2} and P_{RA} and the remaining maxima in P_{AS} are well within 10 percent of one of the observed estimates. It is interesting to note that P_{RA} lags both P_{AS} and P_{Q2} in four of the six disturbances. This phase shift may indicate storage of water in thick stratiform clouds associated with squall lines as discussed by Houze (1977). The values of P_{AS} during undisturbed periods show generally good agreement with P_{RA} except during 12 September when agreement with P_{Q2} is somewhat better. The correlations between the time series are as follows: P_{AS} and P_{RA}, .868; P_{AS} and P_{Q2}, .877; P_{Q2} and P_{RA}, .817. We conclude that the precipitation rates predicted using Eq. (8) agree with observations to within observational uncertainty.

We now compare a similar time series (Fig. 16) of precipitation rates calculated from Eq. (8) <u>but with the l.h.s.</u> $(\frac{dA}{dt})$ <u>equal to zero</u>, i.e. these results are obtained using the cloud work function quasi-equilibrium closure hypothesis. Comparing Figs. 16 and 15, we see that the individual precipitation rates differ by less than 10 percent in almost all instances. P_{AS} in this case is 12.2 mm day^{-1}, only 0.1 mm day^{-1} smaller than the case in which the quasi-equilibrium condition was not used. This result is interpreted as strong supporting evidence for the cloud work function quasi-equilibrium assumption.

Fig. 17 is a time series of the mass flux distribution function, $\mathcal{M}_B(i)$, in units of 10^{-1} mb hr^{-1}. The ordinate is the cloud top pressure, $\hat{p}$,

_____

[1]Times are denoted by the day and hour (GMT) in the form day/hour.

for each sub-ensemble. The dashed line at 1 mb hr^{-1} separates two different contour intervals of 0.2 mb hr^{-1} for $m_B(i) < 1.0$ mb hr^{-1} and 0.4 mb hr^{-1} for $m_B(i) > 1.0$ mb hr^{-1}. There is a distinct bimodal structure in the cloud base mass flux during the disturbed times of September 2nd, 5th, 12th and 17th, but during the weaker disturbance of the 9th September the mass flux distribution function is unimodal. The largest mass fluxes for deep clouds occur at hour 18 on September 2, 4 and 18 when the deep cloud forcing is strongest. The deepest clouds occur at 14/0 corresponding to one of the highest rainfall rates during this 18 day period.

Maximum values in the mass flux of shallow clouds (cloud top detrainment levels below 800 mb) tend to occur in the wakes of the strongest disturbances. For example, the deep convection of the 2nd and 17th of September is immediately followed by a sharp change in the peak mass flux toward shallow clouds. The mass flux into the shallow clouds increases over a period of about 12 hours before diminishing. The shallow clouds occur during both undisturbed and disturbed conditions; a notable exception is on 9 September when very weak upward motion was observed at low levels and the mass flux distribution is unimodal.

Figure 18 shows the time-averaged mass flux distribution (mb hr^{-1}) as a function of cloud top pressure. The distribution has two peaks for 400 and 800 mb clouds and a secondary maximum for 600 mb clouds. These results differ considerably from the results of many diagnostic studies which show highly bimodal distributions with very little mass flux into middle level clouds. The mass flux distribution spectrum obtained in diagnostic studies has a large mass flux into shallow clouds to satisfy the observed large-scale thermodynamical budgets. However, the results shown in Figure 18 are predicted

using the cloud work function quasi-equilibrium and the predicted large-scale thermodynamical budgets do not necessarily satisfy the observed budgets.

Let us define "predicted" values of the large-scale heat source and moisture sink as

$$(Q_1 - Q_R)_{AS} \equiv c_p [\frac{\partial \overline{T}}{\partial t}]_{CU},$$ (15)

and

$$(Q_2)_{AS} \equiv - L[\frac{\partial \overline{q}_v}{\partial t}]_{CU},$$ (16)

where $[\frac{\partial \overline{T}}{\partial t}]_{CU}$ and $[\frac{\partial \overline{q}_v}{\partial t}]_{CU}$ are the large-scale warming and drying by cumulus clouds given by the underlined terms in Eqs.(1) and (2). Furthermore, let the total (sensible plus latent) eddy heat flux convergence due to clouds be given by

$$(Q_1 - Q_2 - Q_R) = c_p[\frac{\partial \overline{T}}{\partial t}]_{CU} + L[\frac{\partial \overline{q}_v}{\partial t}]_{AS}.$$ (17)

Figure 19 shows the predicted and observed values of $(Q_1 - Q_2 - Q_R)$ in units of ^oC day^{-1} as a function of height (mb). The values of Q_R were taken from Dopplick (1970). We see that the total heat flux convergence above 400 mb is underestimated and between 600 and 800 mb it is overestimated. Therefore, although the net heating in the vertical air column (measured by the average precipitation rate) is quite close to observations, the vertical distribution of the heating is not very well predicted. Note that the total heat flux convergence is severely underestimated in the 100 mb layer above cloud base. It is possible that underprediction of the transport by very shallow cumulus clouds by this parameterization is responsible for this discrepancy with observations.

Figures 20 and 21 show the separate time-averaged predicted and observed $Q_1 - Q_R$ and Q_2. We see that there is net cooling due to cumulus clouds above 300 mb and net moistening above 400 mb. Between 300 and 600 mb, the warming due to the deeper clouds is underestimated and below 650 mb it is overestimated. The drying predicted by the parameterization is under-estimated above 700 mb and overestimated below 750 mb. These results show that the time-averaged changes in temperature and moisture predicted by the parameterization are not well simulated level by level. However, we see that the vertically integrated changes are close to the time-averaged observations.

The dashed lines in Figure 20 and 21 represent a modification of the above heat and moisture budgets by allowing precipitation produced at cloud top levels above the freezing level to evaporate into the large-scale environ-ment below the freezing level. This modification does not of course, alter the total eddy heat flux convergence shown in Figure 19. Inclusion of evapor-ation produces a noticeable redistribution of the heating and moistening in the vertical air column. Overprediction of cooling and moistening in the upper layers is reduced as is the overprediction of warming and drying in the lower layers.

We have performed similar calculations of predicted precipitation rates and cumulus warming and drying using the moist convective adjustment scheme of Manabe et al (1965) and the parameterization of Kuo (1965). The values of large-scale moisture convergence are known from the observations so that application of Kuo's scheme is quite straight forward. Precipitation rates from the moist convective adjustment scheme were calculated in the following manner. First, the observed large-scale environment was adjusted to a moist adiabatically neutral state whenever the observed relative exceeded a critical

value $(R_H)_C$. Second, the observed large-scale processes were used to modify the neutral state. Finally, the precipitation rates were calculated by readjusting the modified state to a neutral state while maintaining the constant $(R_H)_C$. Several different values of $(R_H)_C$ were used. Obviously, if $(R_H)_C = 100\%$, then no precipitation would be predicted since the large-scale environment was not saturated over the GATE area.

Table 1 shows the time averaged precipitation rates $\tilde{P}_{Q2}$, $\tilde{P}_{AS}$ and the averages predicted by Kuo's scheme $(\tilde{P}_{KUO})$ and the moist convective adjustment $(\tilde{P}_{MCA})$ for different values of $(R_H)_C$. We see that the precipitation rates predicted by Kuo's scheme and the moist convective adjustment scheme for $(R_H)_C \geq 80\%$ are considerably smaller than observed estimates.

Table 2 summarizes the correlation coefficients between the various schemes for predicting cumulus precipitation discussed in this paper. $(R_H)_C = 70\%$ is used for P_{MCA}. There is a large, though not frequent, noise in P_{MCA} resulting from the arbitrary critical relative humidity criterion. This noise is largely responsible for the low correlations of P_{MCA} with P_{Q2} and P_{RA}. P_{KUO} is highly correlated with P_{Q2}. Since the observed moisture changes in the tropics are usually quite small compared to the large-scale moisture convergence, this high correlation is not surprising.

Tables 3 and 4 show the values of predicted cumulus warming and drying as a function of height for Kuo's parameterization and the moist convective adjustment. These values should be compared with the values shown in Figs. 20 and 21. Kuo's scheme predicts a monotonic increase in warming with height up to a maximum value at 350 mb. The drying predicted by Kuo's scheme resembles the observed Q_2 but is underpredicted. The warming predicted by the moist convective adjustment is characterized by large noise due to the critical

relative humidity criterion. Similar noise is found in the predicted moisture changes due to cumulus clouds.

From the results presented in this paper, we conclude that the Arakawa-Schubert cumulus parameterization is very successful in predicting the precipitation rates over the GATE area during Phase III. The precipitation rates are not changed substantially by the inclusion of a $\frac{dA}{dt}$ term in Eq. (8), thereby providing a strong verification of the cloud work function quasi-equilibrium in this situation. There are discrepancies with observations in the predicted vertical distributions of warming and drying due to cumulus clouds. Future research will be aimed at correcting these deficiencies. Kuo's scheme and the moist convective adjustment were shown to be quite unsuccessful in predicting precipitation and cumulus warming and drying over the GATE area.
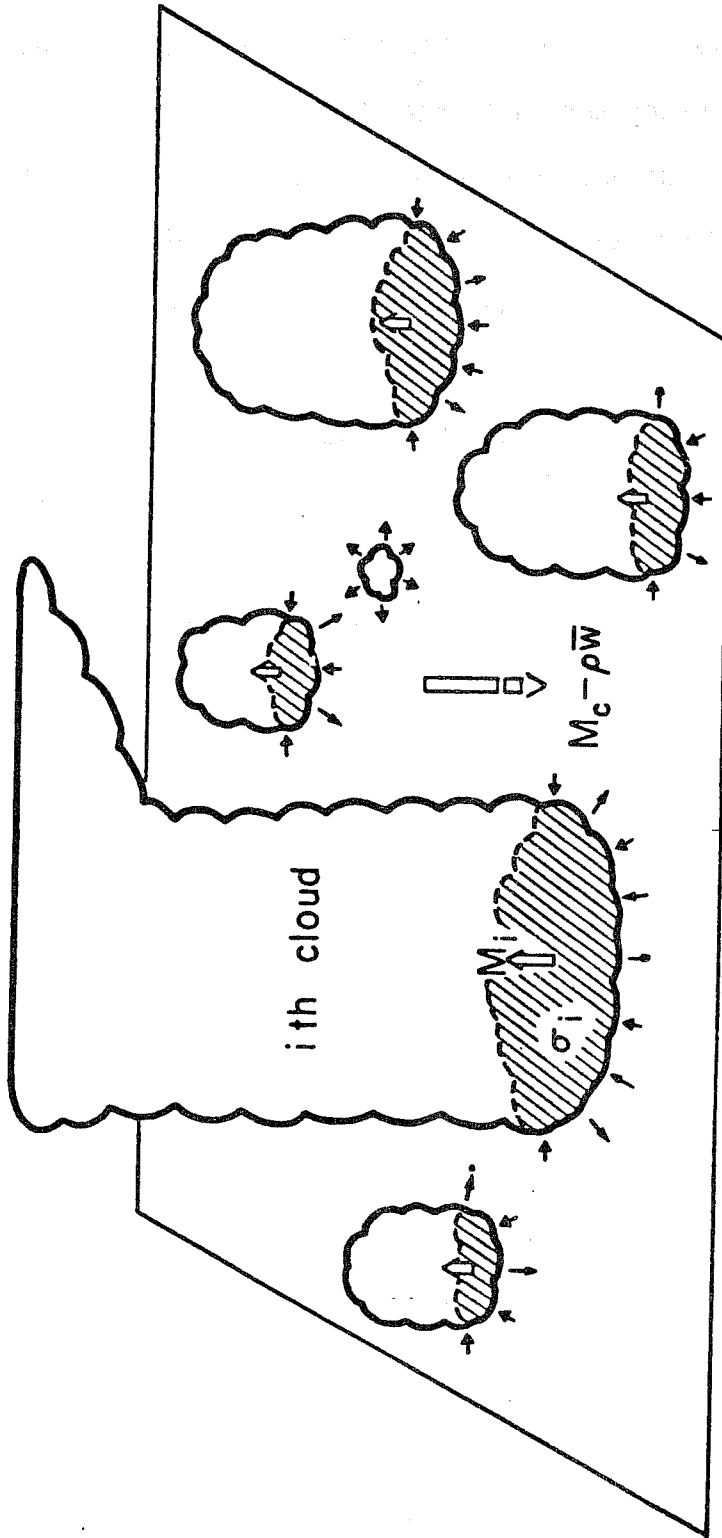
Fig. 1. A unit horizontal area at some level z between the lowest cloud base and the highest cloud top. Clouds penetrating this level entrain air from the environment during their growth and mature states and detrain air during their mature and decaying stages. One cloud that has lost buoyancy is shown detraining cloud air into the environment. σ_i is the fractional area of the ith cloud.

$$M_c(KF+1/2, i) = \mathcal{M}_B(i)$$
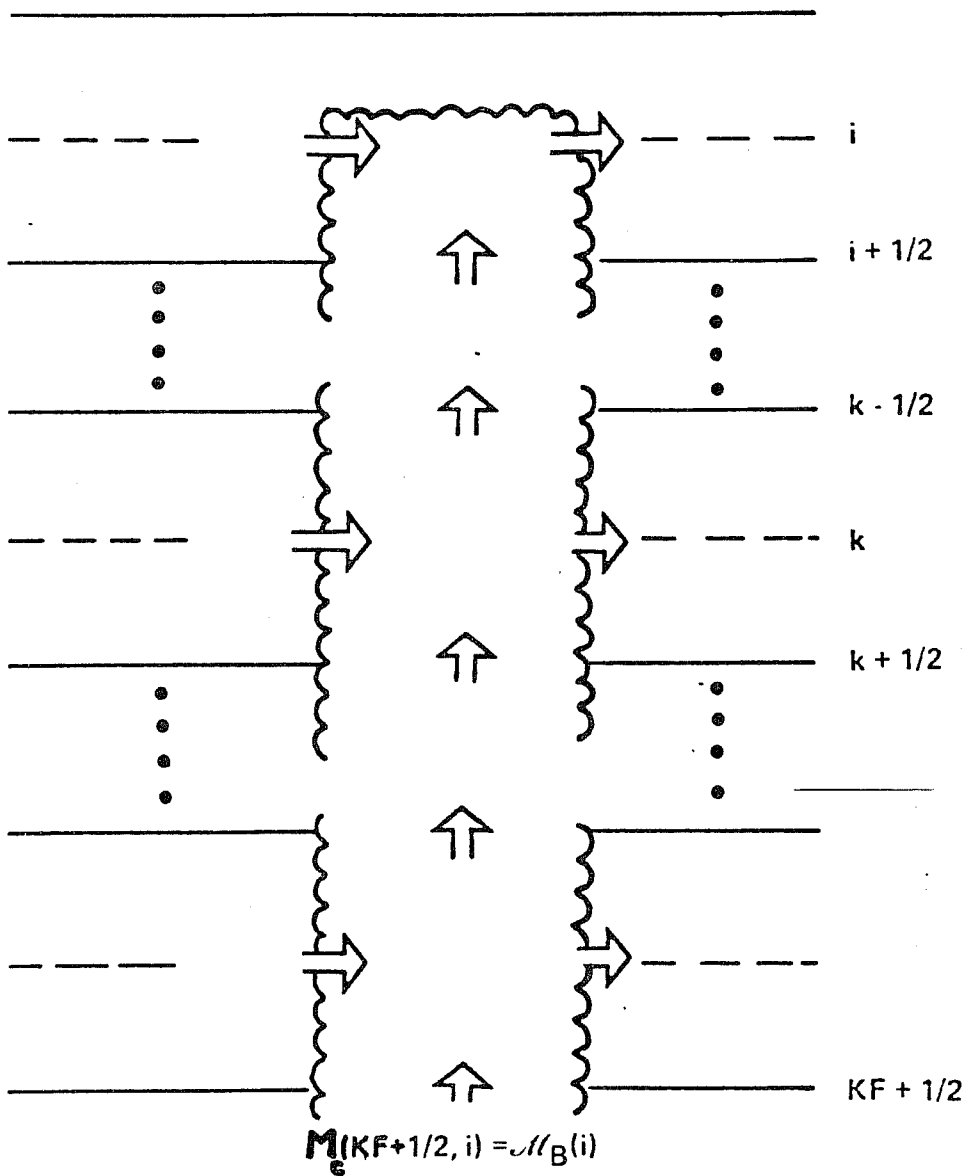
Fig. 2. The vertical structure of the ith cloud type. Entrainment and detrainment from the cloud lateral edges take place at all integer levels penetrated by the cloud top including the cloud top level. The sub-ensemble vertical mass flux, M_c, is normalized at cloud base (level KF +1/2).
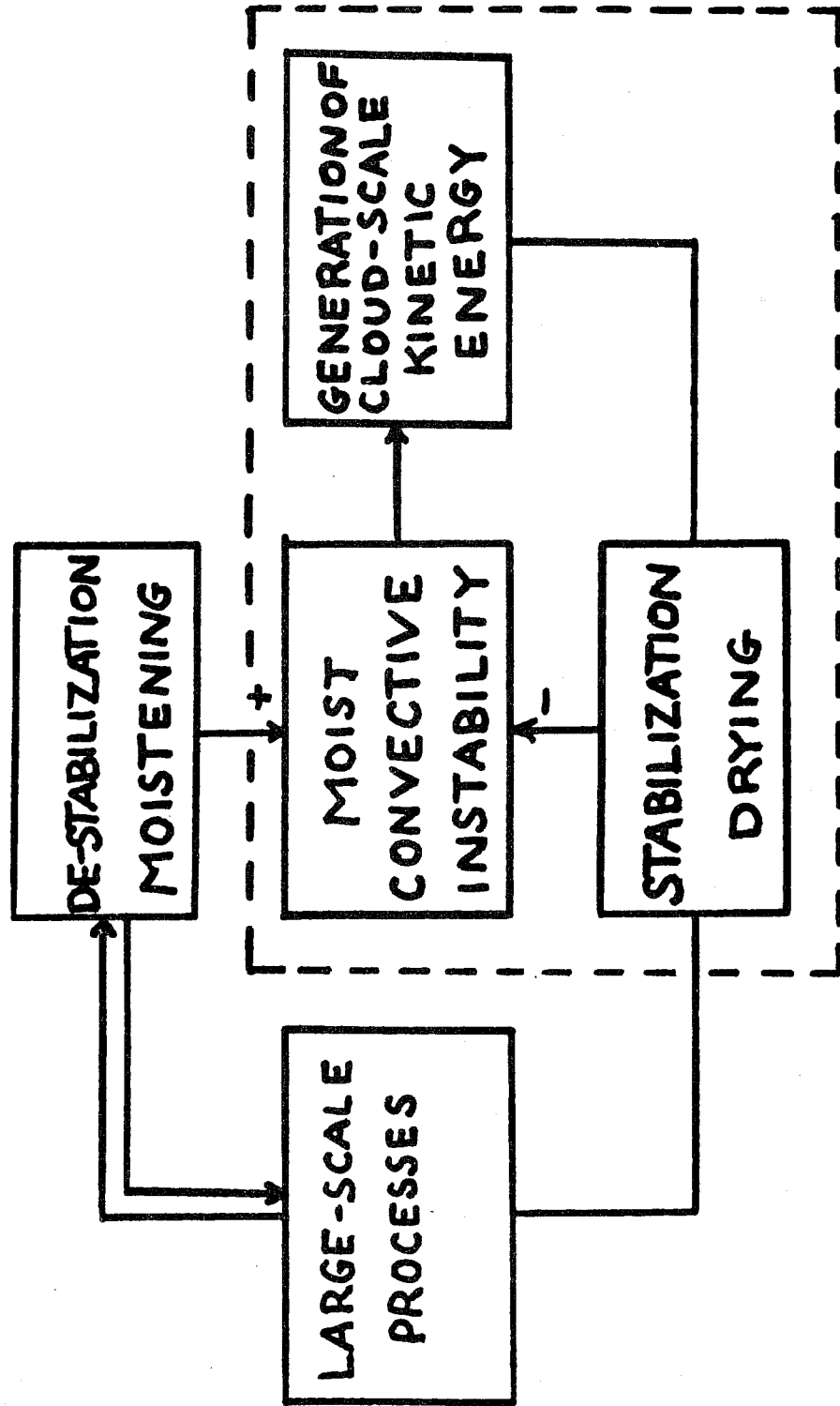
Fig. 3. A schematic diagram of the physical basis for the closure assumption of the Arakawa-Shubert cumulus parameterization.

Fig. 4. A time series of the large-scale cloud layer forcing for each sub-ensemble from 1-18 September. The ordinate is the cloud top pressure, p.

CLOUD LAYER FORCING   (KJ/KG/DAY)

CONTOUR INTERVAL = 1.0
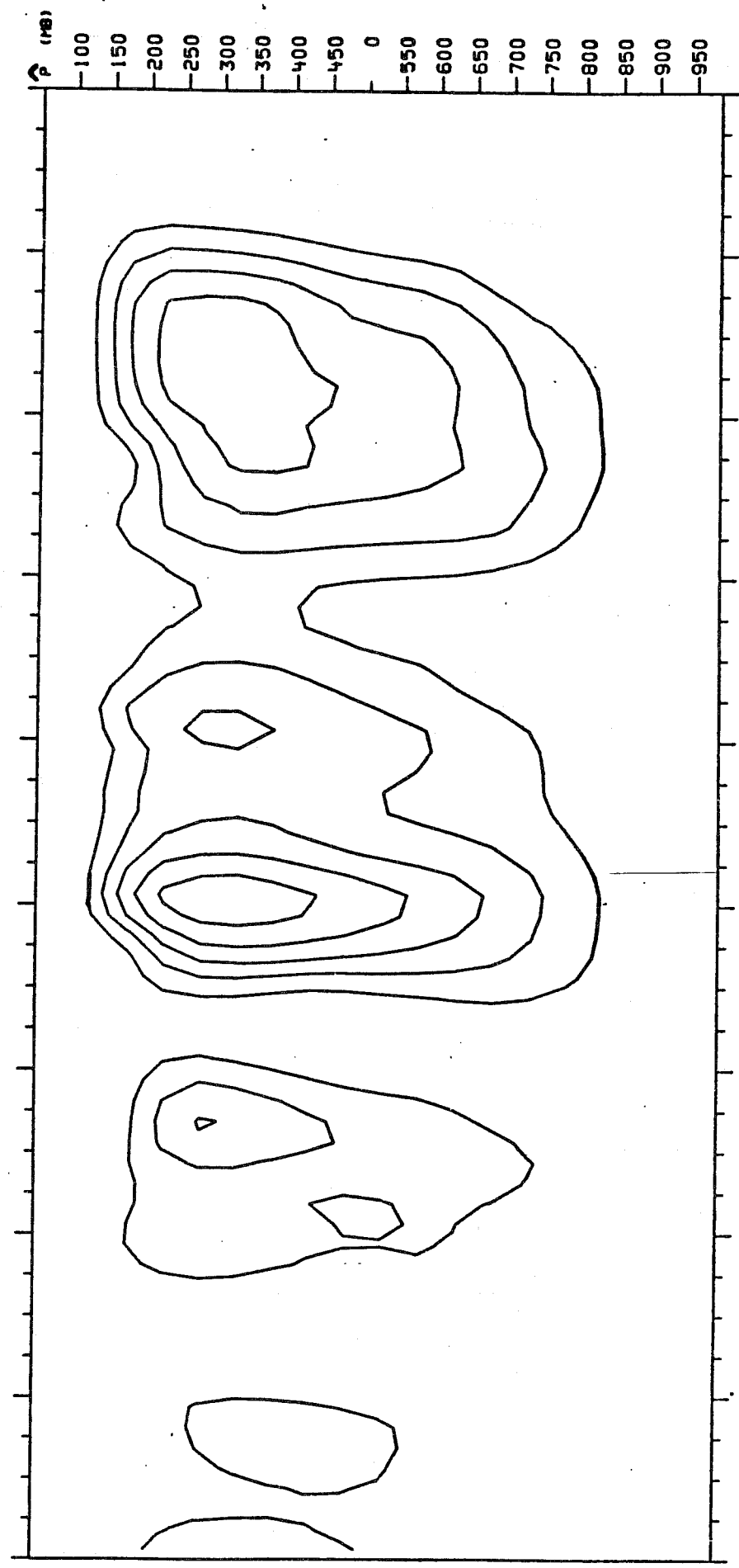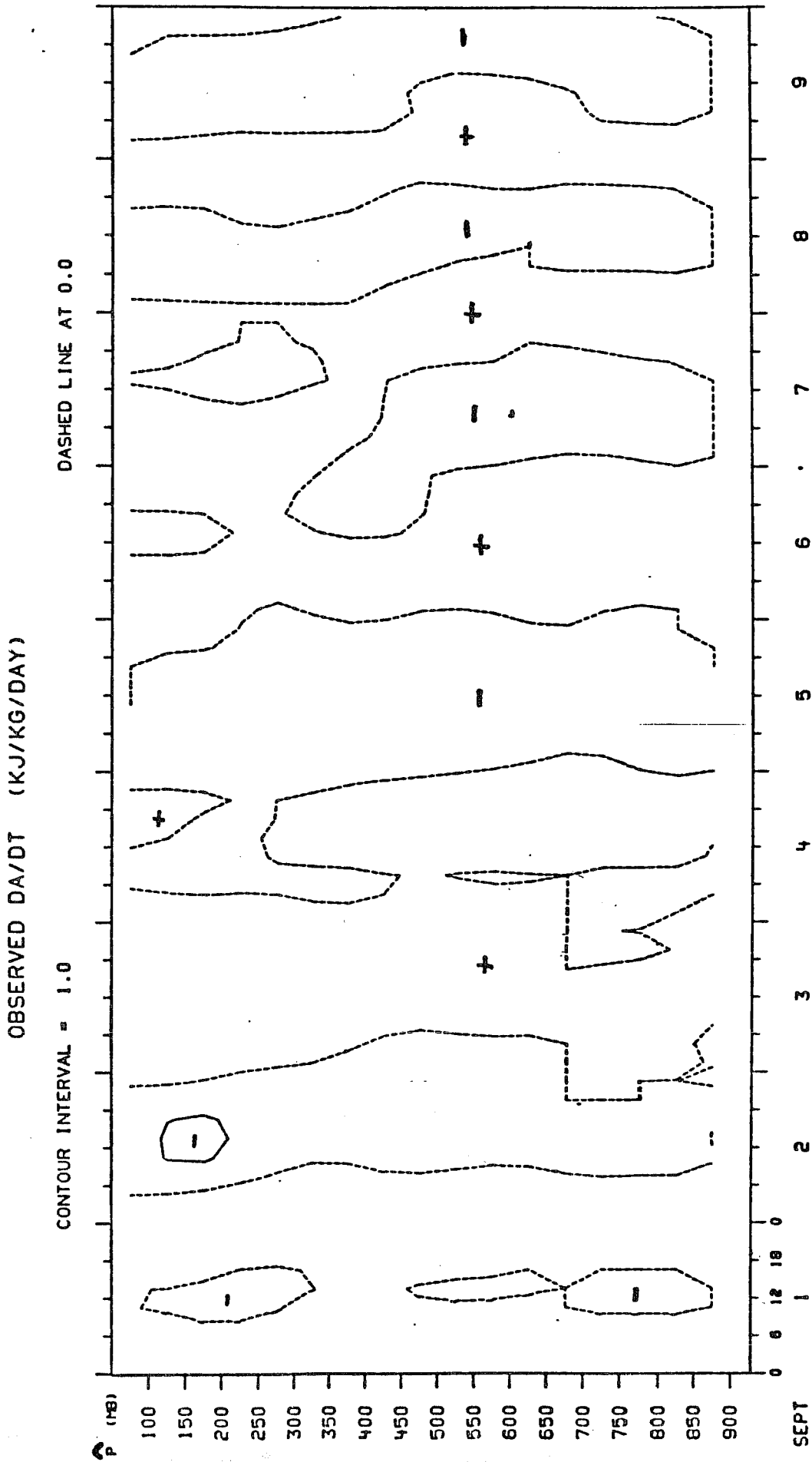
Fig. 4. (continued)

Fig. 5. A time series of the observed time change of the cloud work function for each sub-ensemble.

OBSERVED DA/DT (KJ/KG/DAY)

DASHED LINE AT 0.0

CONTOUR INTERVAL = 1.0
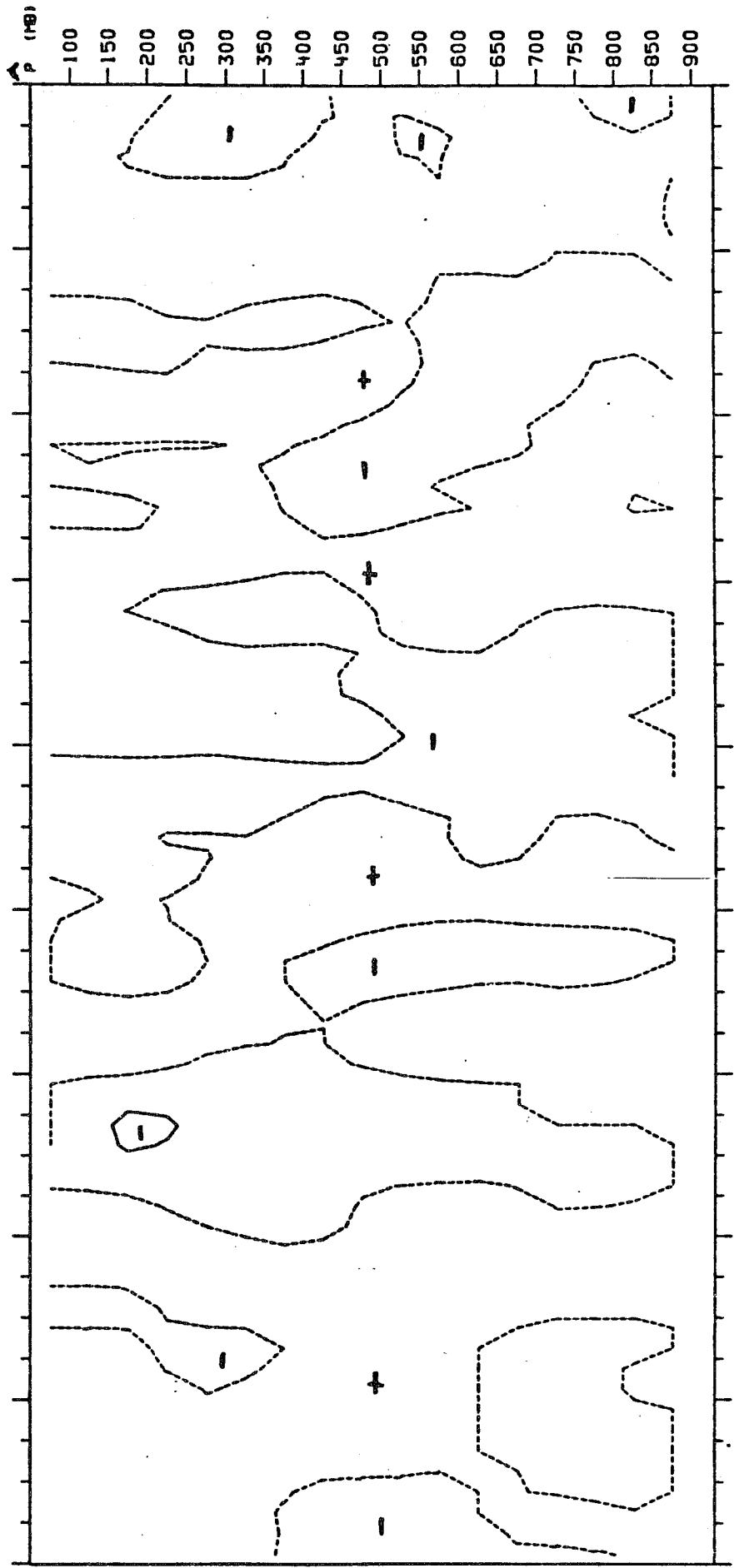
Fig. 5. (continued)
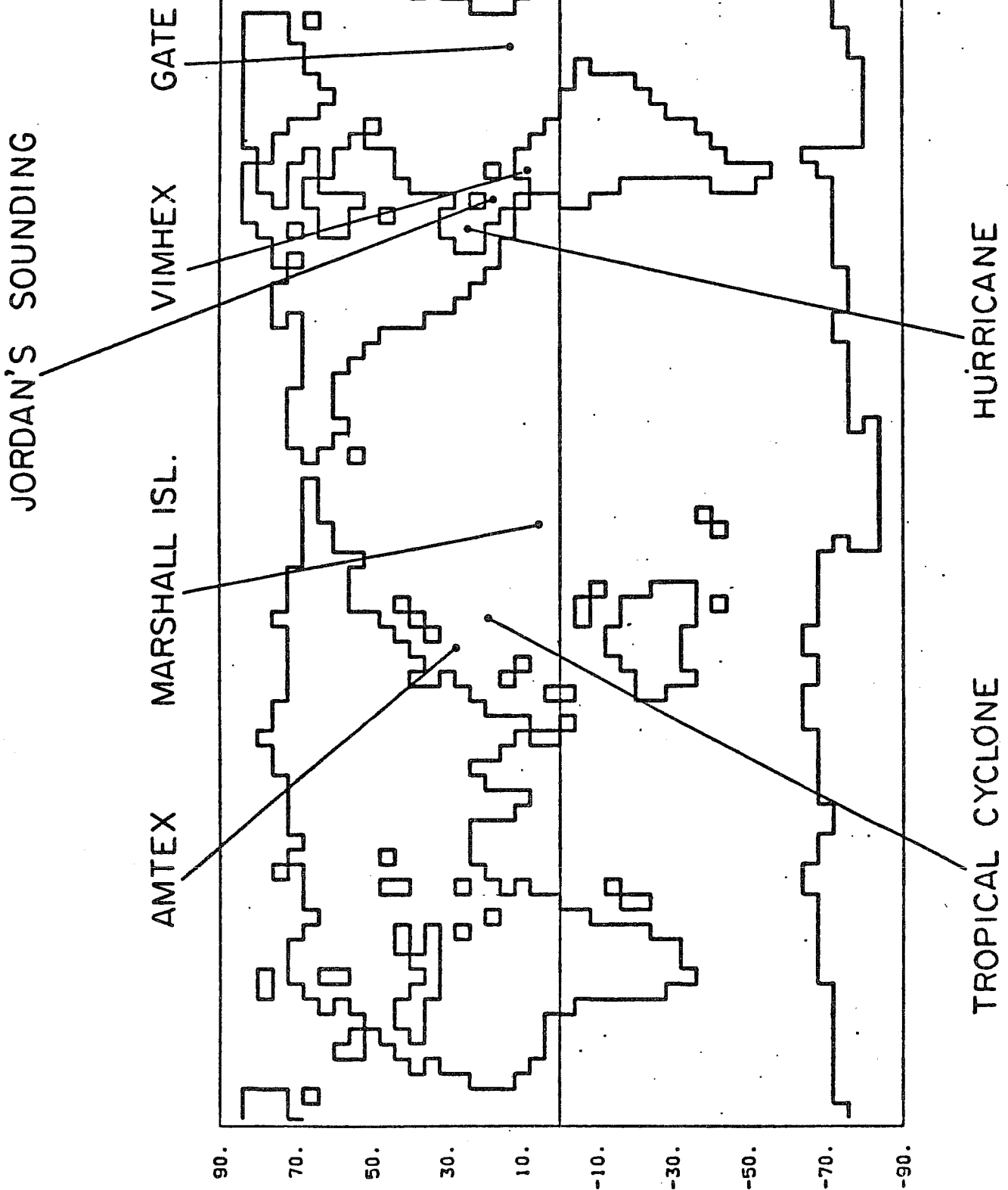
Fig. 6. Locations of the data used for calculating the cloud work functions.
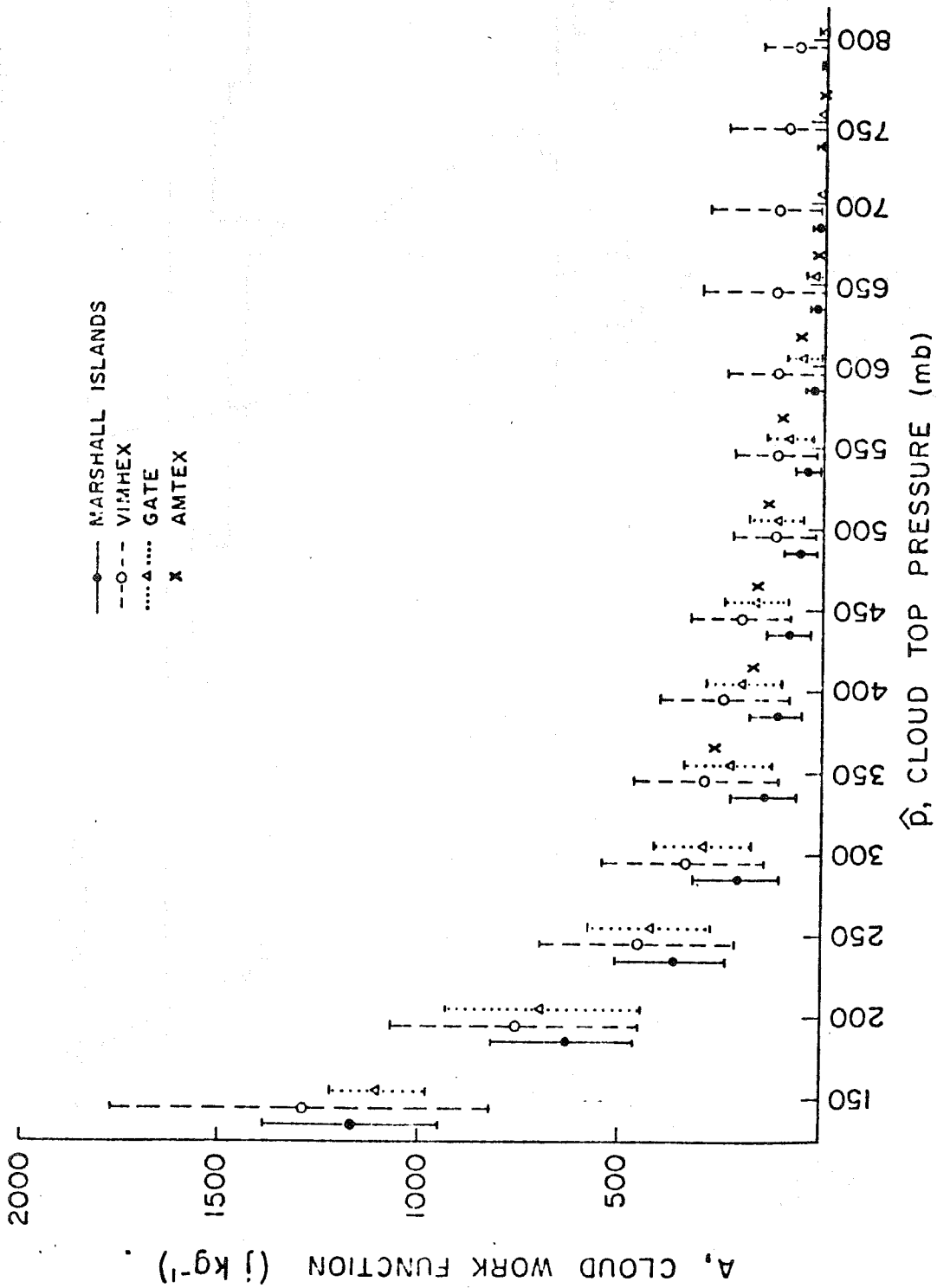
Fig. 7. Mean values and standard deviations of the cloud work functions calculated from Marshall Islands, VIMHEX, GATE and AMTEX data. The abscissa is the cloud top pressure, $\hat{p}$.
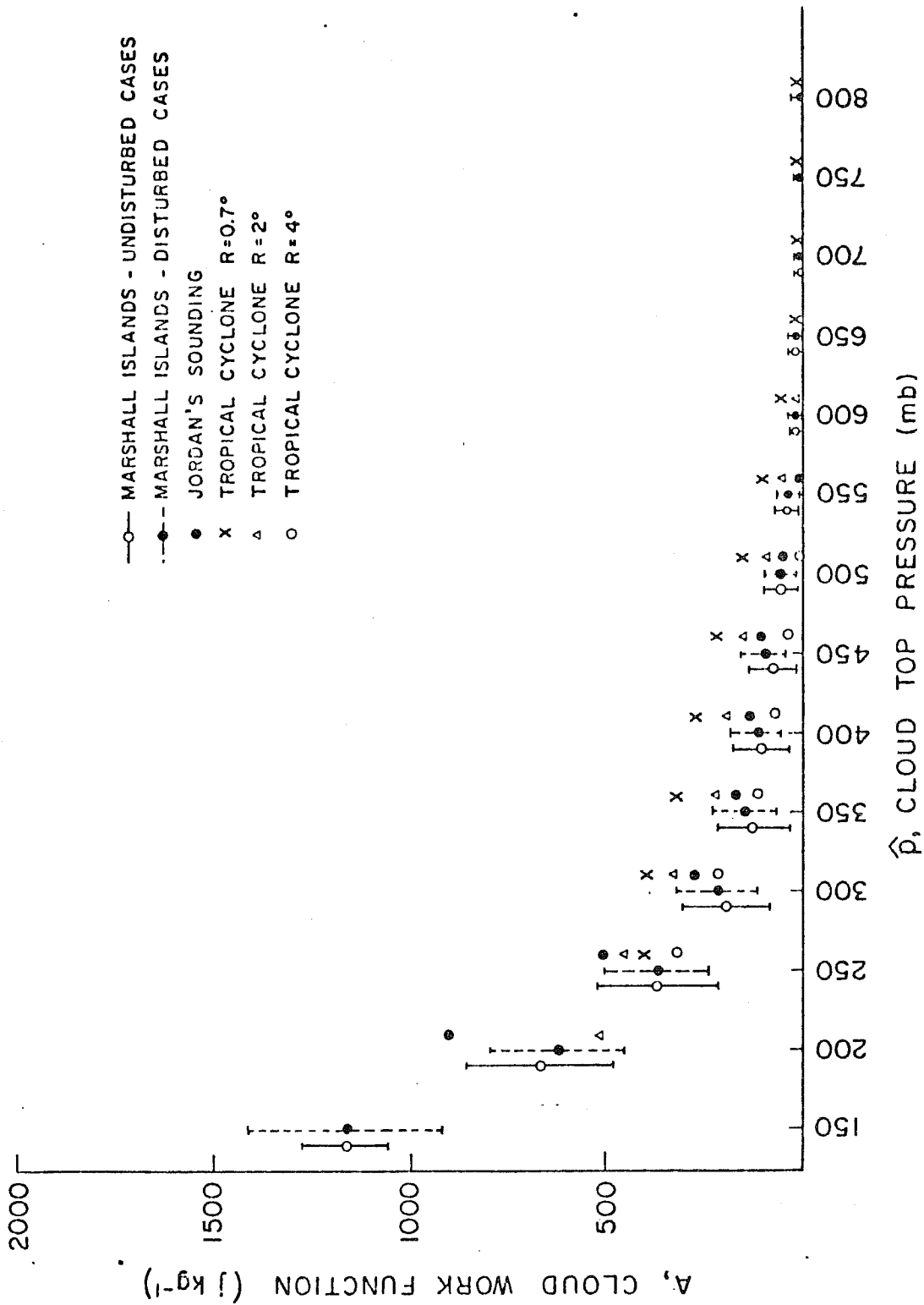
Fig. 8. Same as Fig. 7 for Marshall Islands disturbed and undisturbed cases, Jordan's sounding and tropical cyclone data.
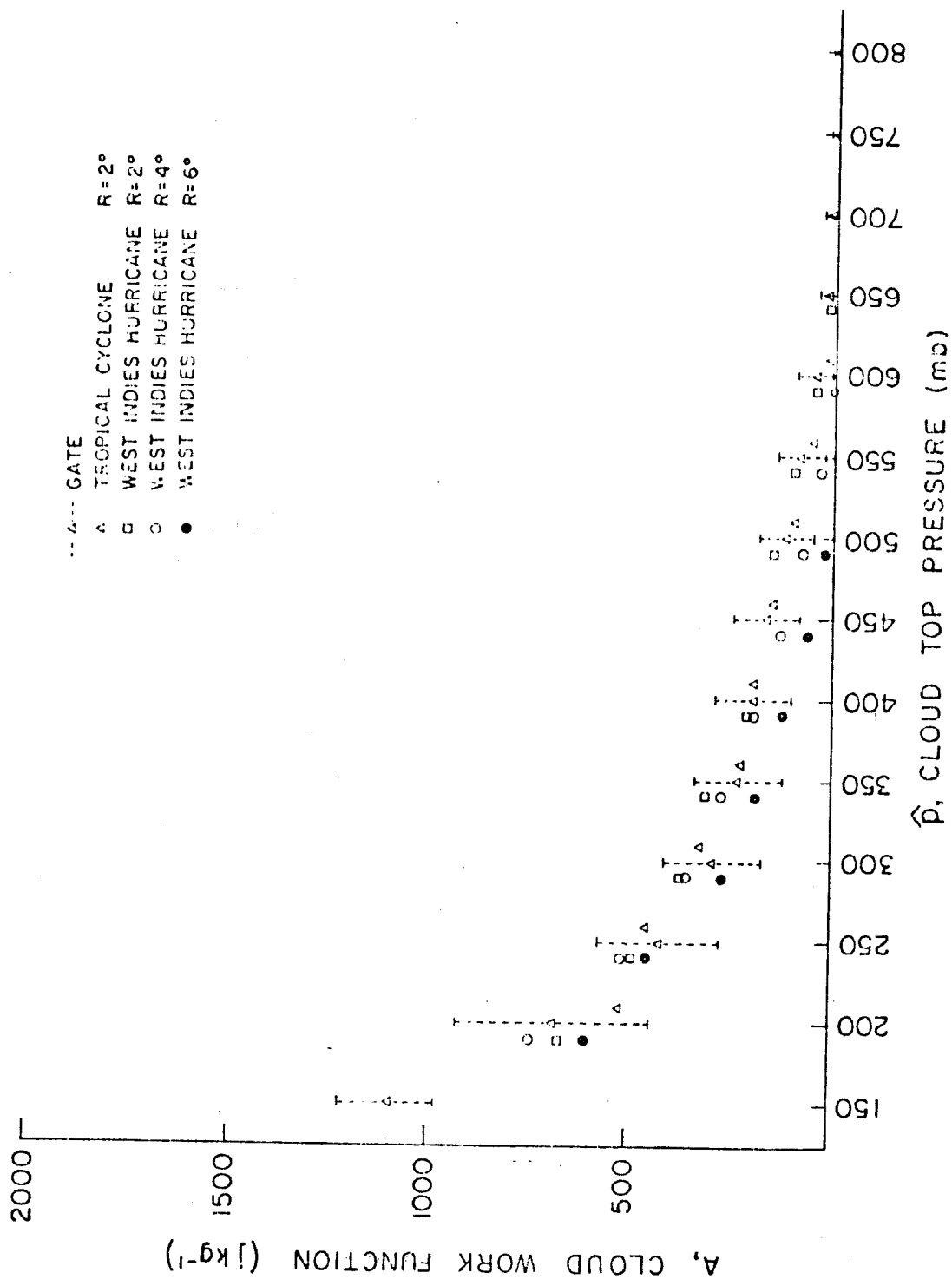
Fig. 9. Same as Fig. 7 for the hurricane data.
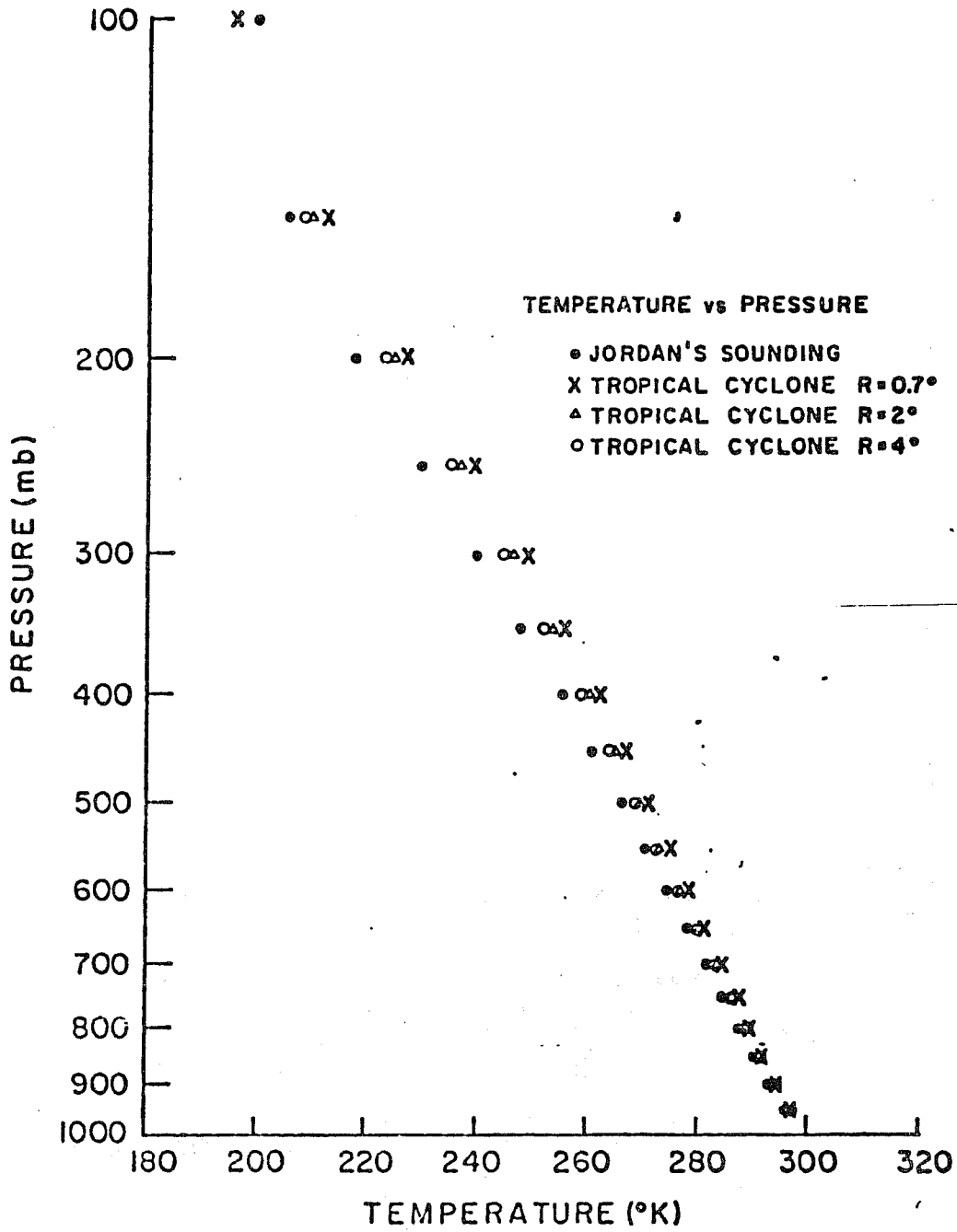
Fig. 10. Temperature vs. pressure for Jordan's sounding and the tropical cyclone data.
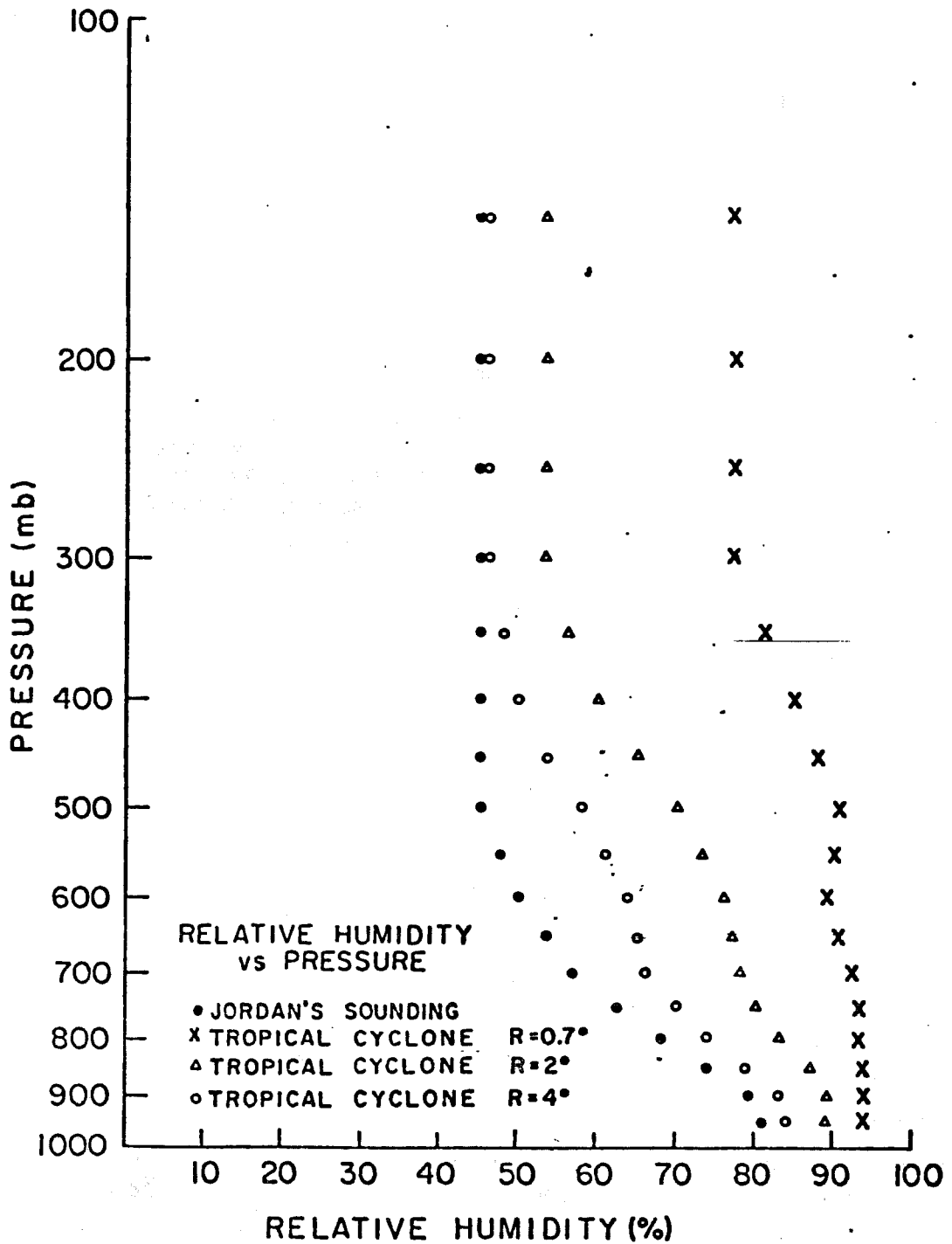
Fig. 11. Relative humidity vs. pressure for Jordan's sounding and the tropical cyclone data.
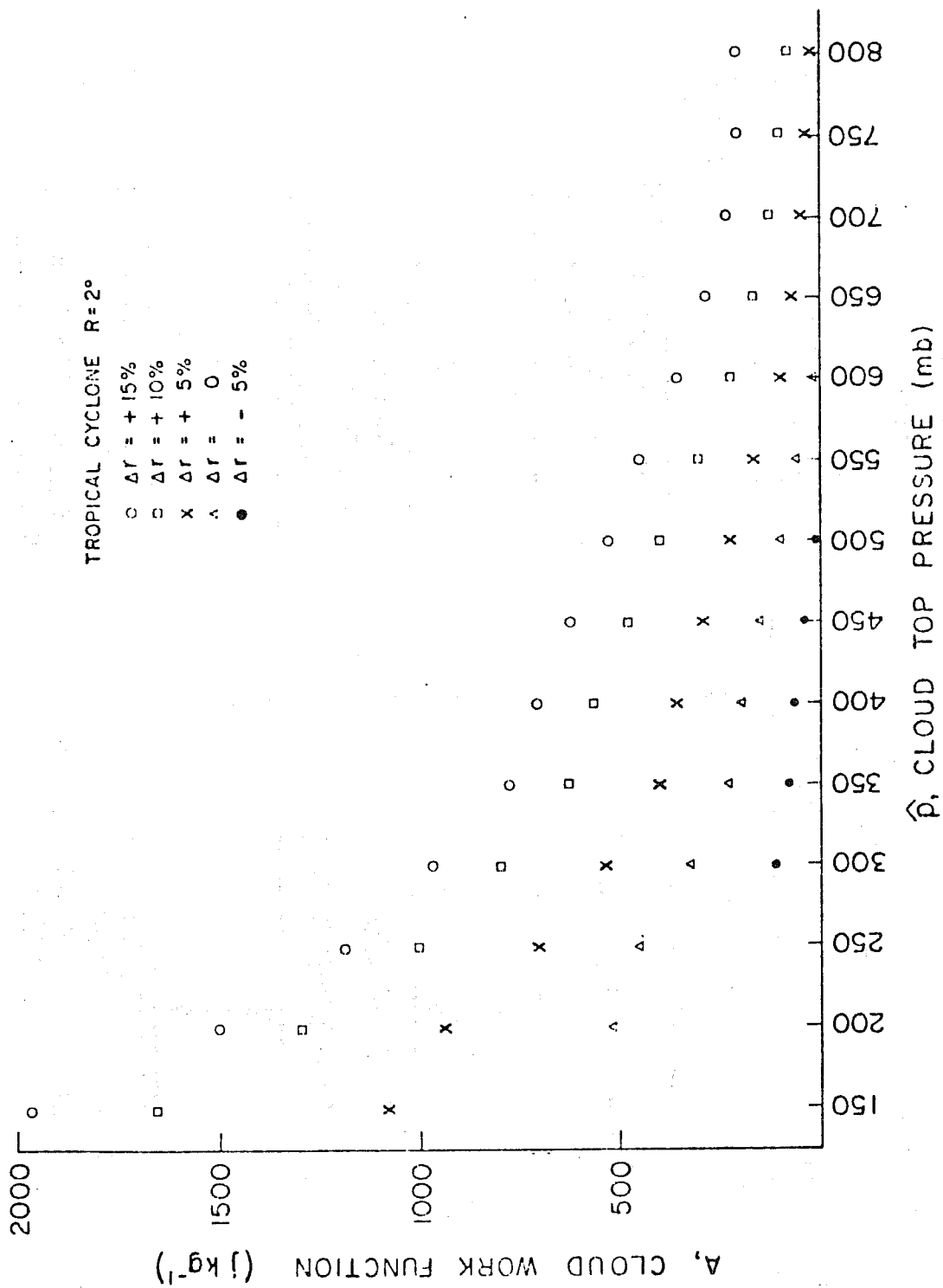
Fig. 12. Same as Fig. 7 but with artificially modified relative humidities.
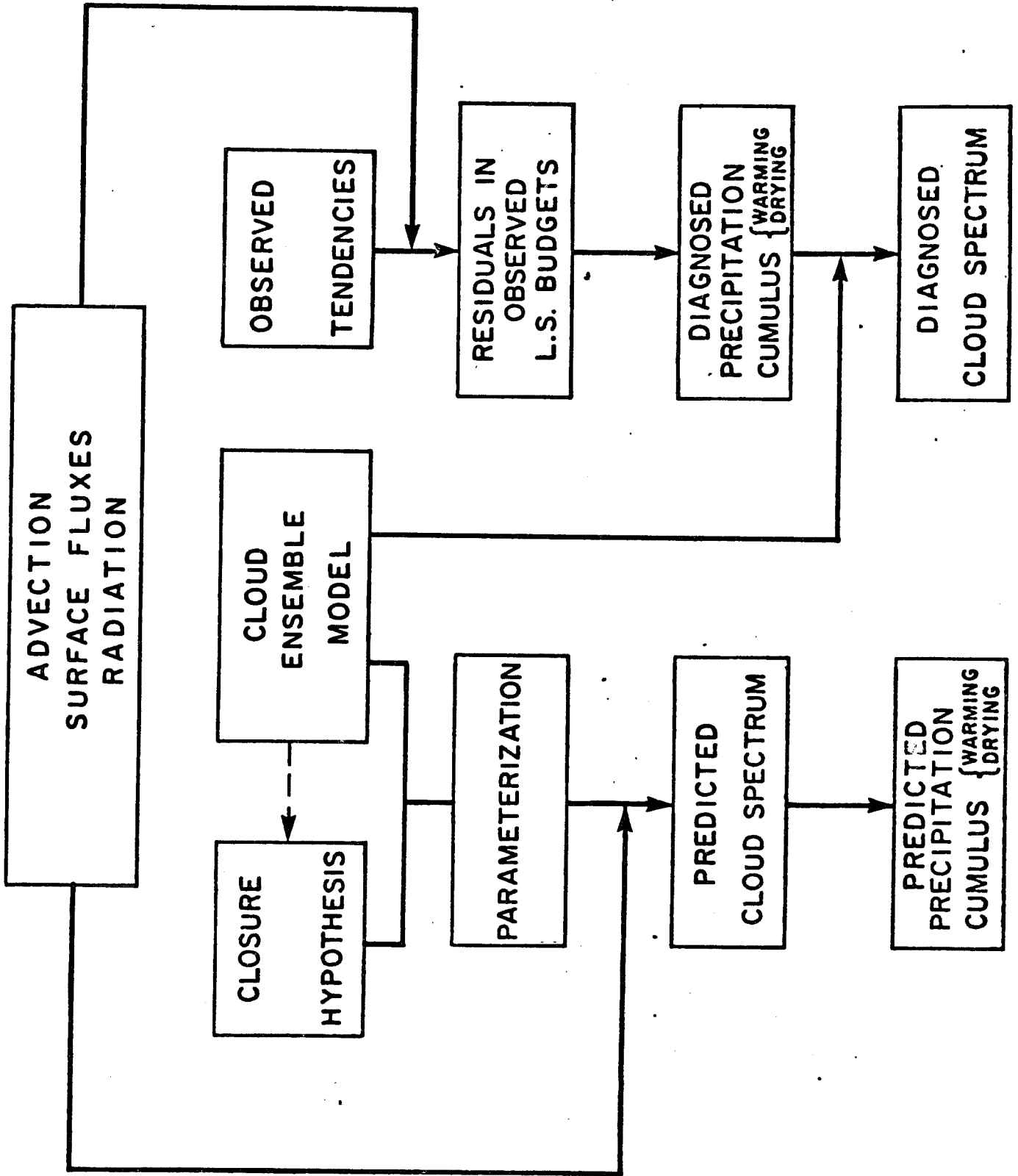
Fig. 13. A schematic diagram illustrating the use of observed data to study
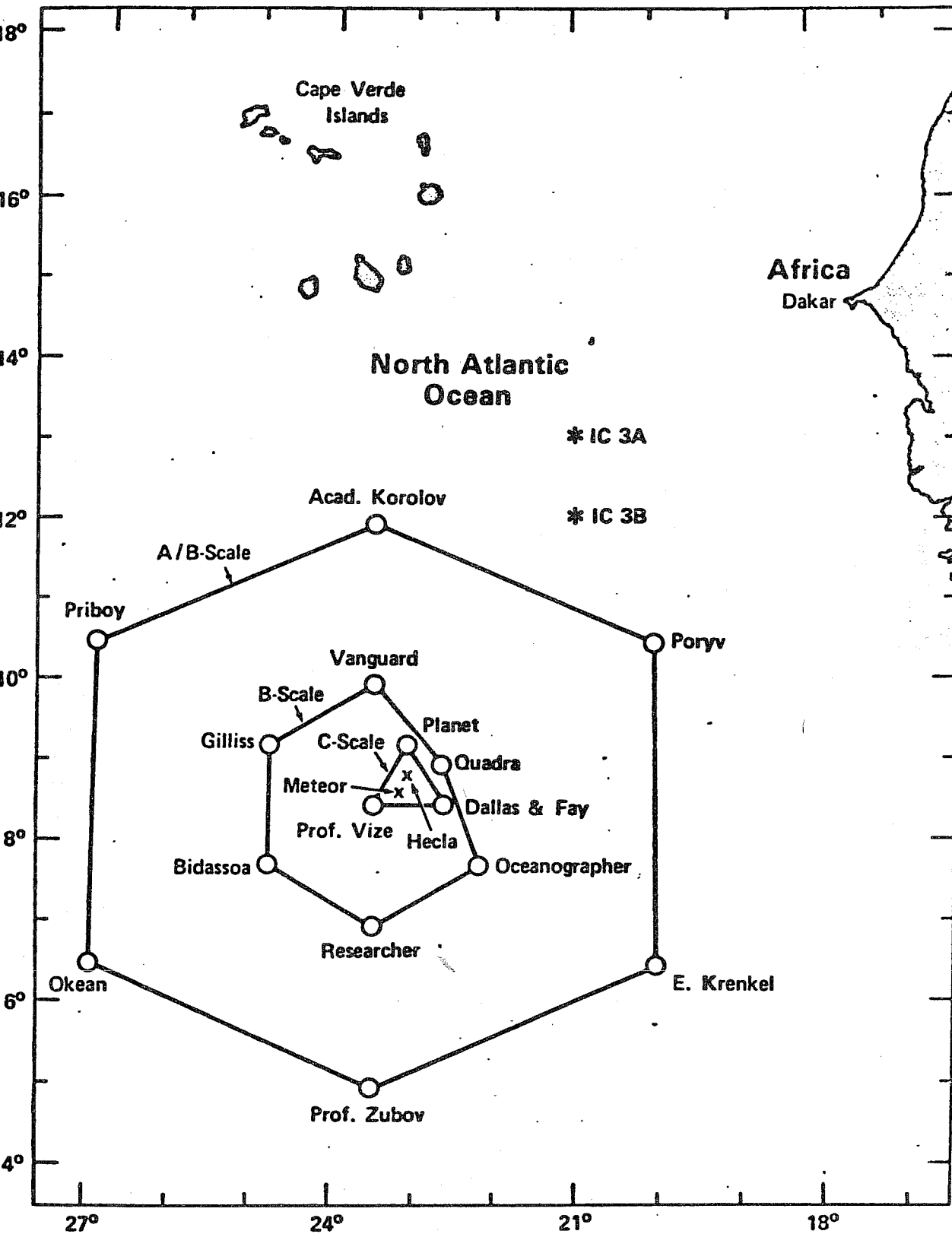
Fig. 14. Ship array during Phase III of GATE.
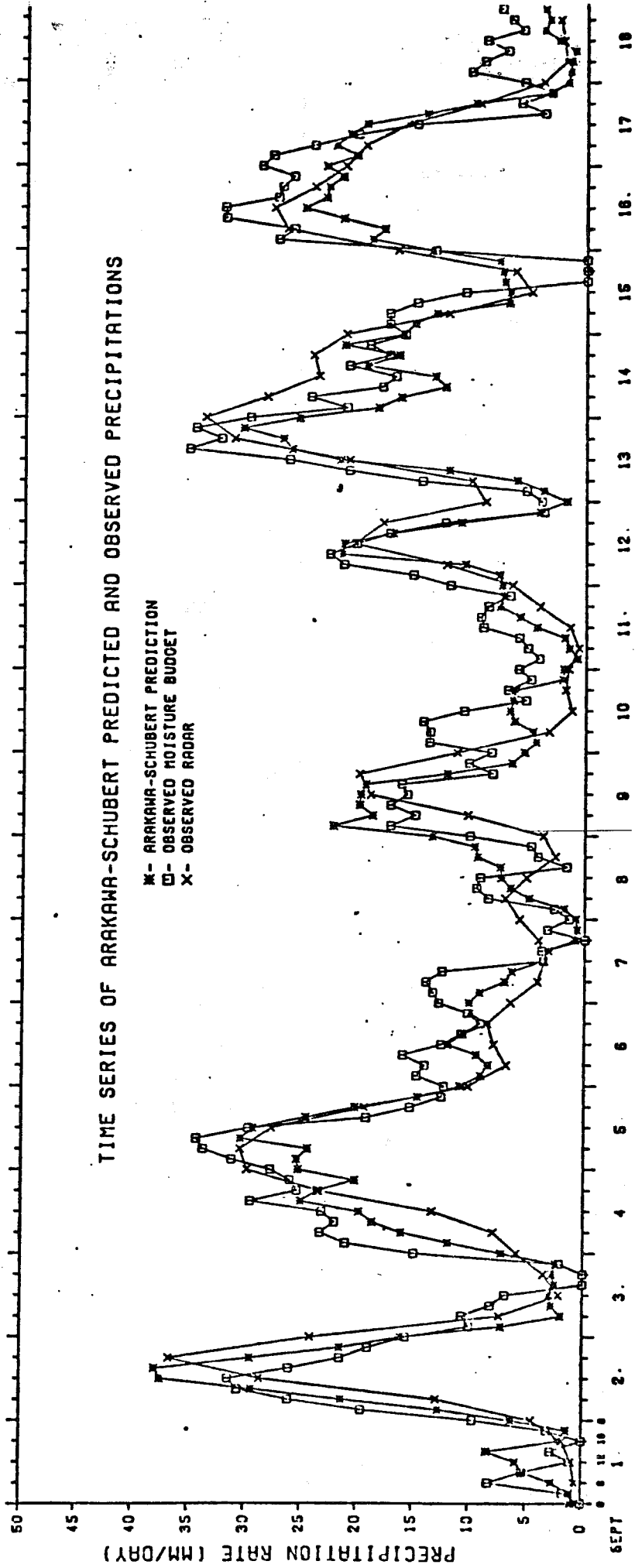
Fig. 15. Time series of precipitation rates (mm day^{-1}) derived from the mass flux distribution function determined by Eq. (8), the observed moisture budget and observed radar measurements.
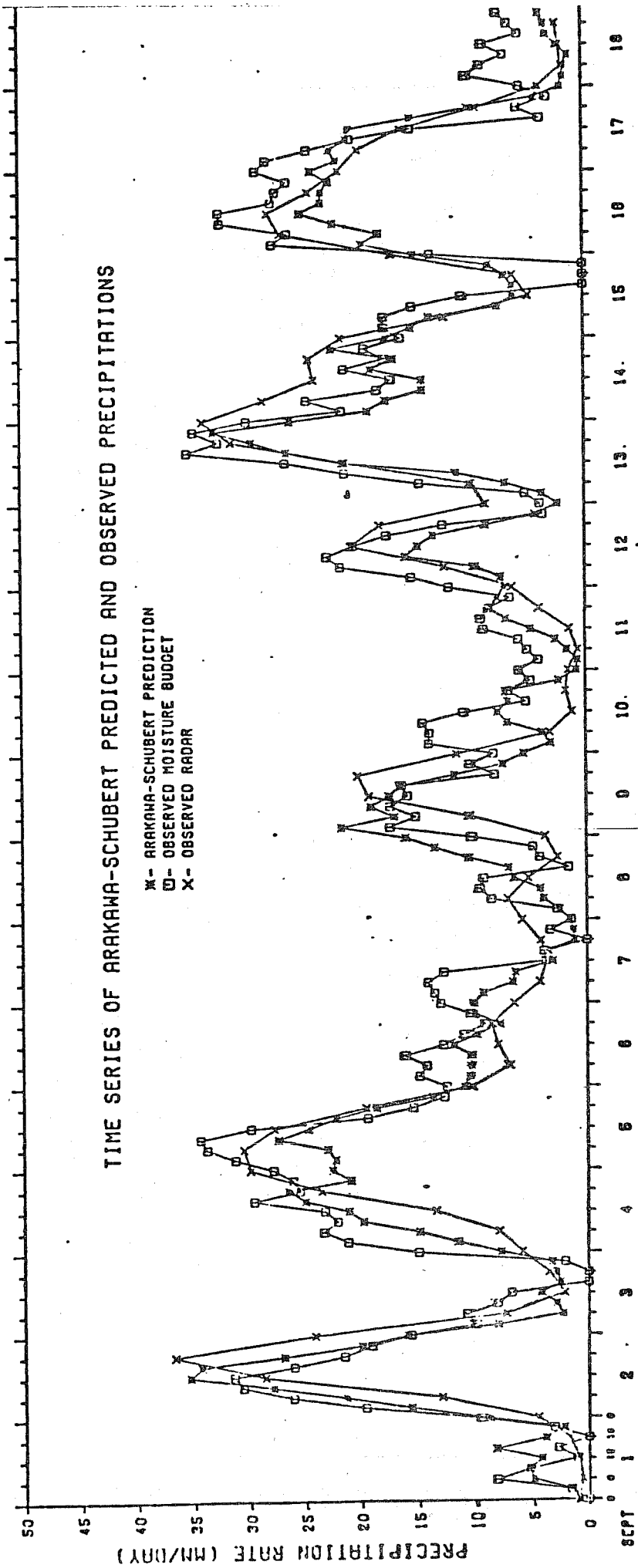
$$\frac{dA}{dt} = 0$$

TIME SERIES OF ARAKAWA-SCHUBERT PREDICTED AND OBSERVED PRECIPITATIONS

⚹- ARAKAWA-SCHUBERT PREDICTION
▣- OBSERVED MOISTURE BUDGET
X- OBSERVED RADAR

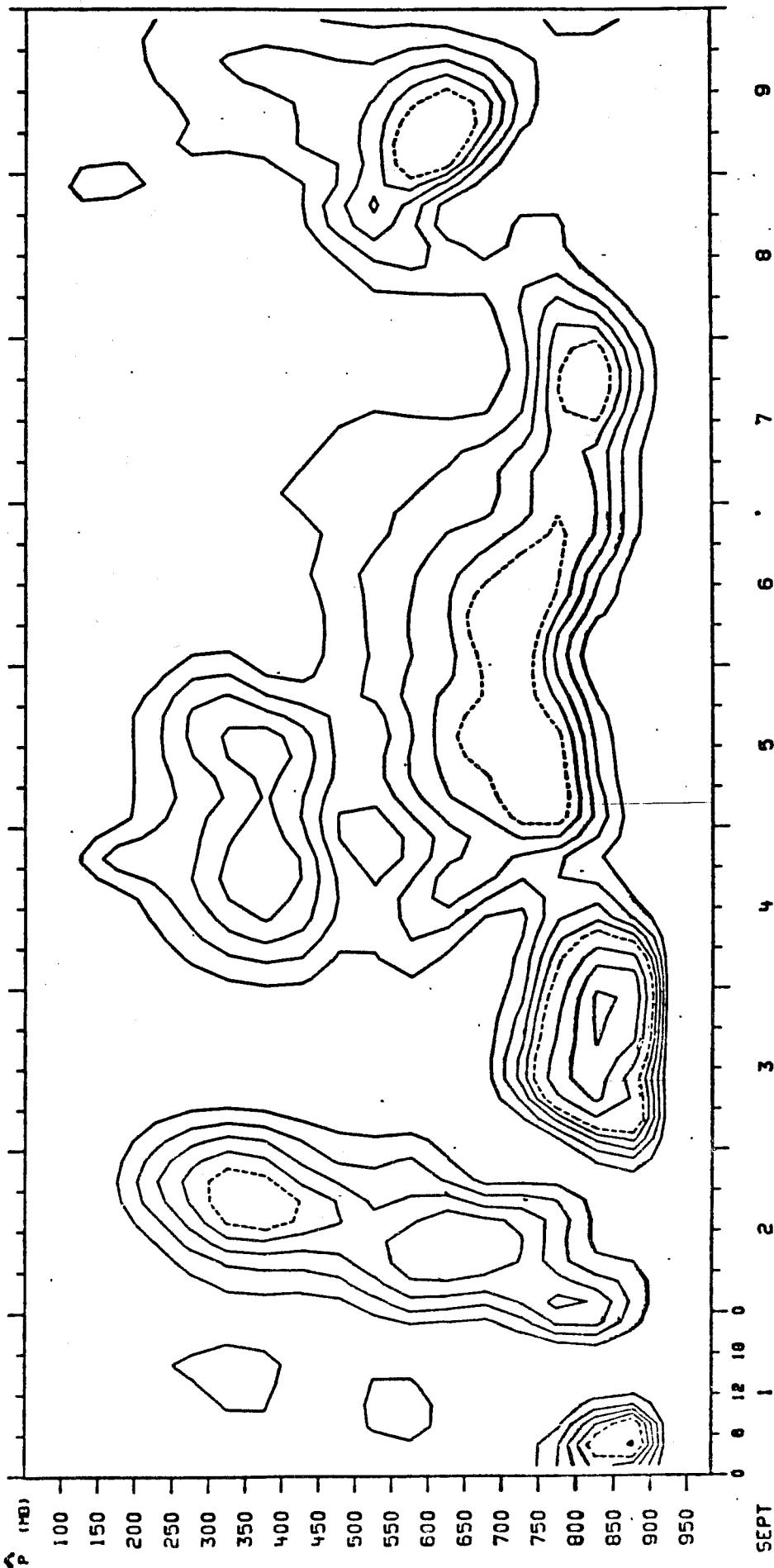Fig. 16. Same as Fig. 15 but with $\frac{dA}{dt} = 0$ in Eq. (8).

Fig. 17. Time series of the mass flux distribution function (mb hr^{-1}). The ordinate is the cloud top pressure, $\hat{p}$.

$$\frac{dA}{dt} = 0$$

MASS FLUX AT CLOUD BASE   (MB/HR)*10.$^{-1}$

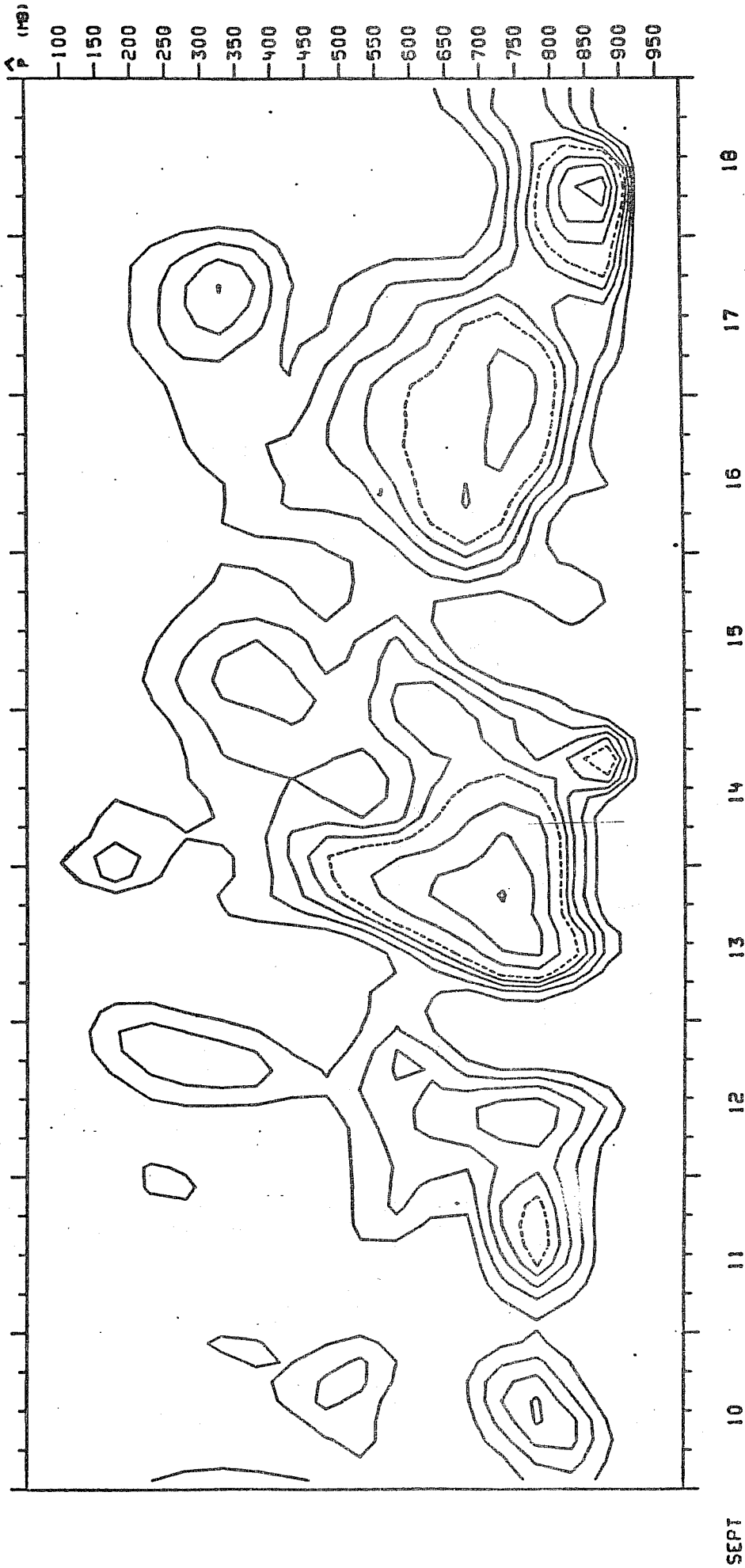CONTOUR INTERVAL = 2.0, 4.0   DASHED LINE AT 10.0

Fig. 17. (continued)
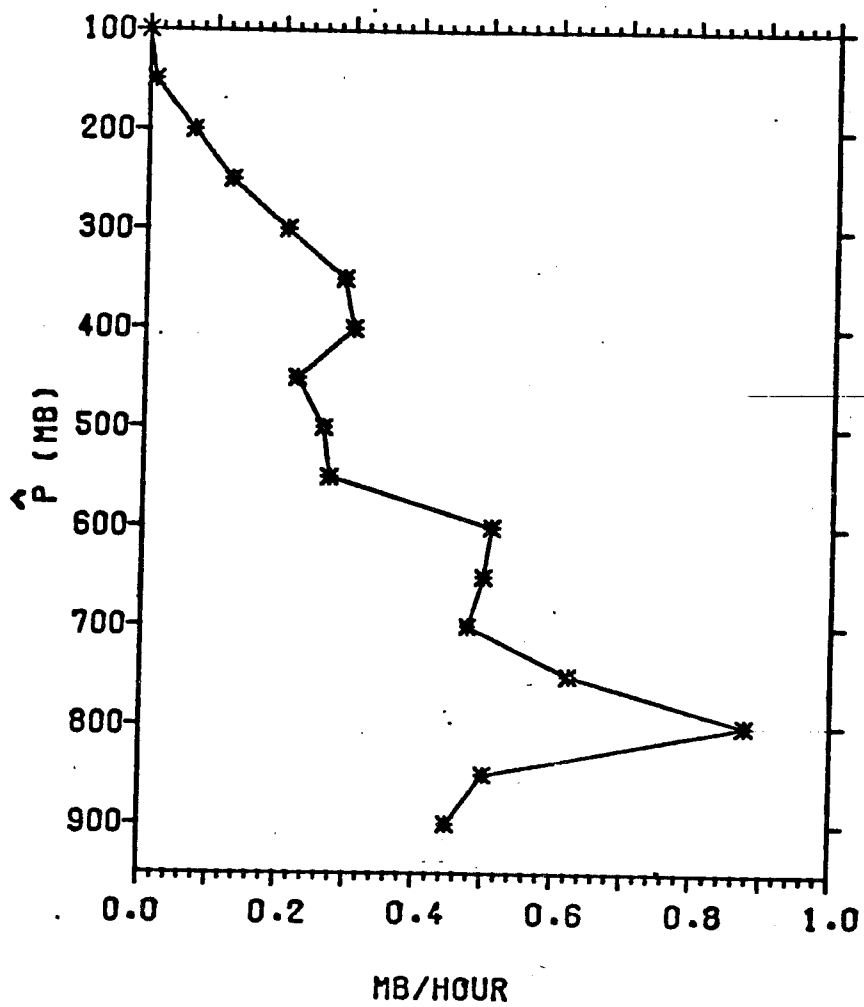
TIME-AVERAGED
MASS FLUX AT CLOUD BASE

Fig. 18. The time-averaged mass flux distribution function (mb hr^{-1}) vs. cloud top pressure.
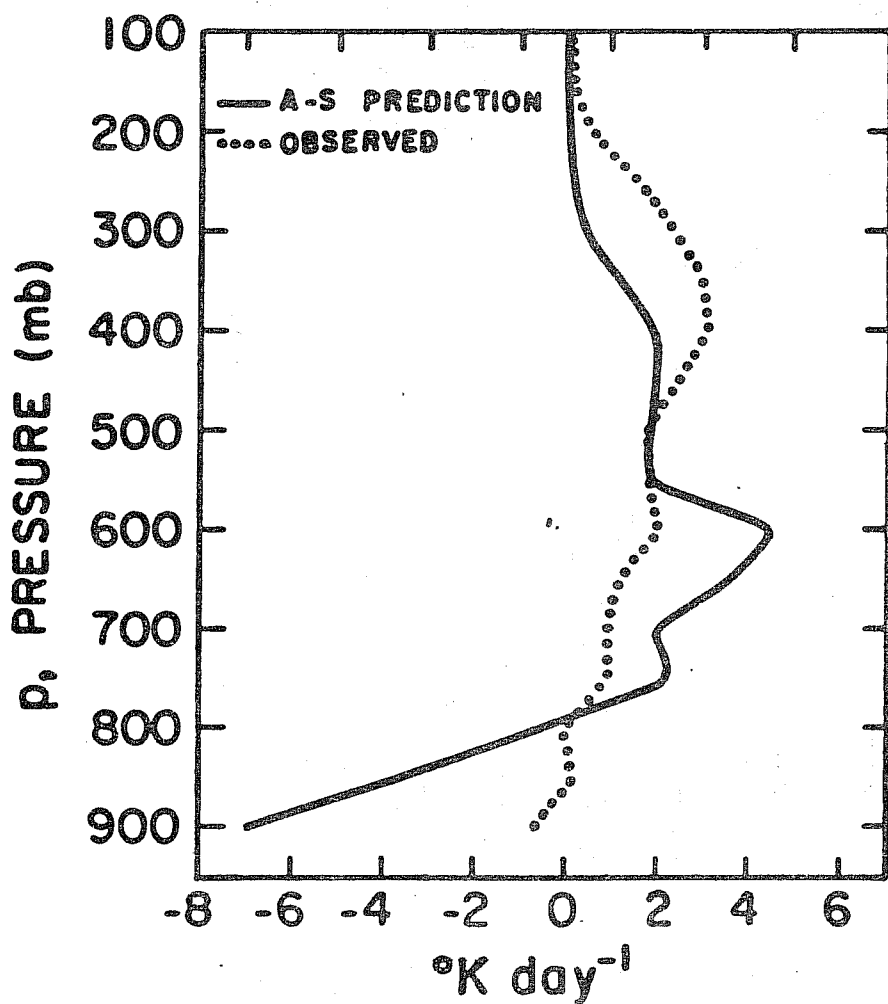
Fig. 19. The predicted and observed $Q_1 - Q_2 - Q_R$ (^oC day^{-1}) vs. pressure (mb).
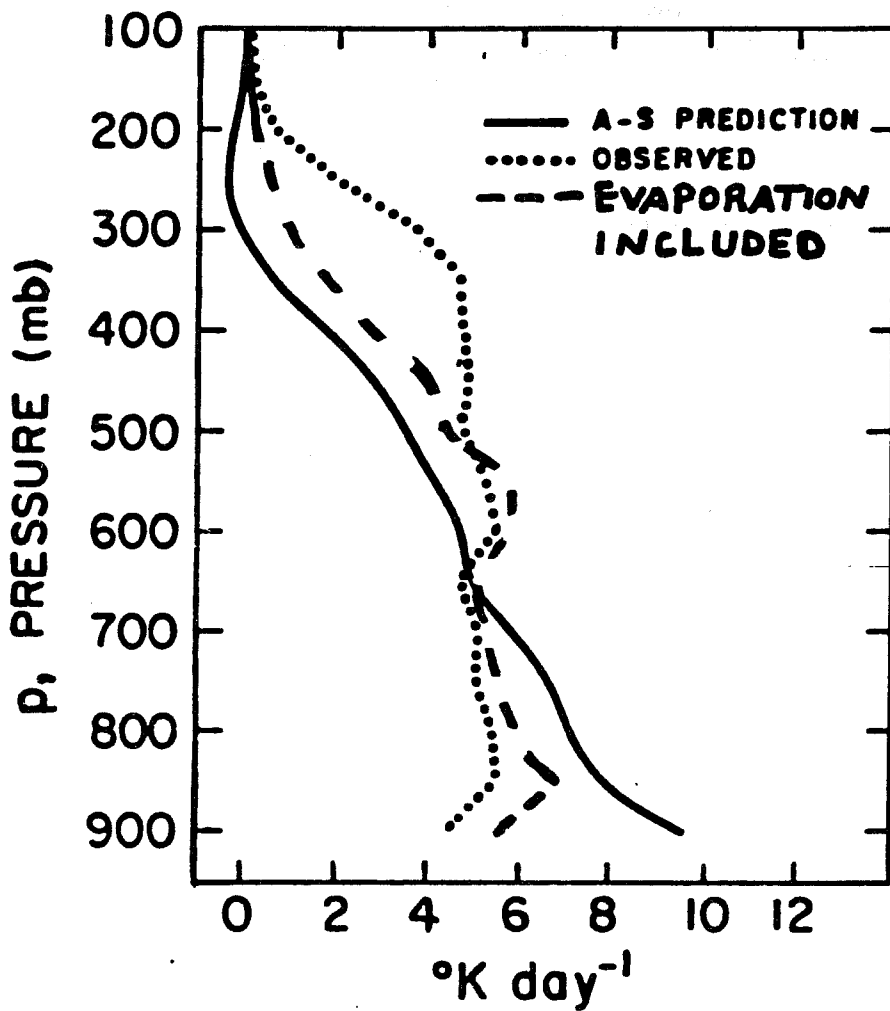
Fig. 20. Same as Fig. 19 for $Q_1 - Q_R$.
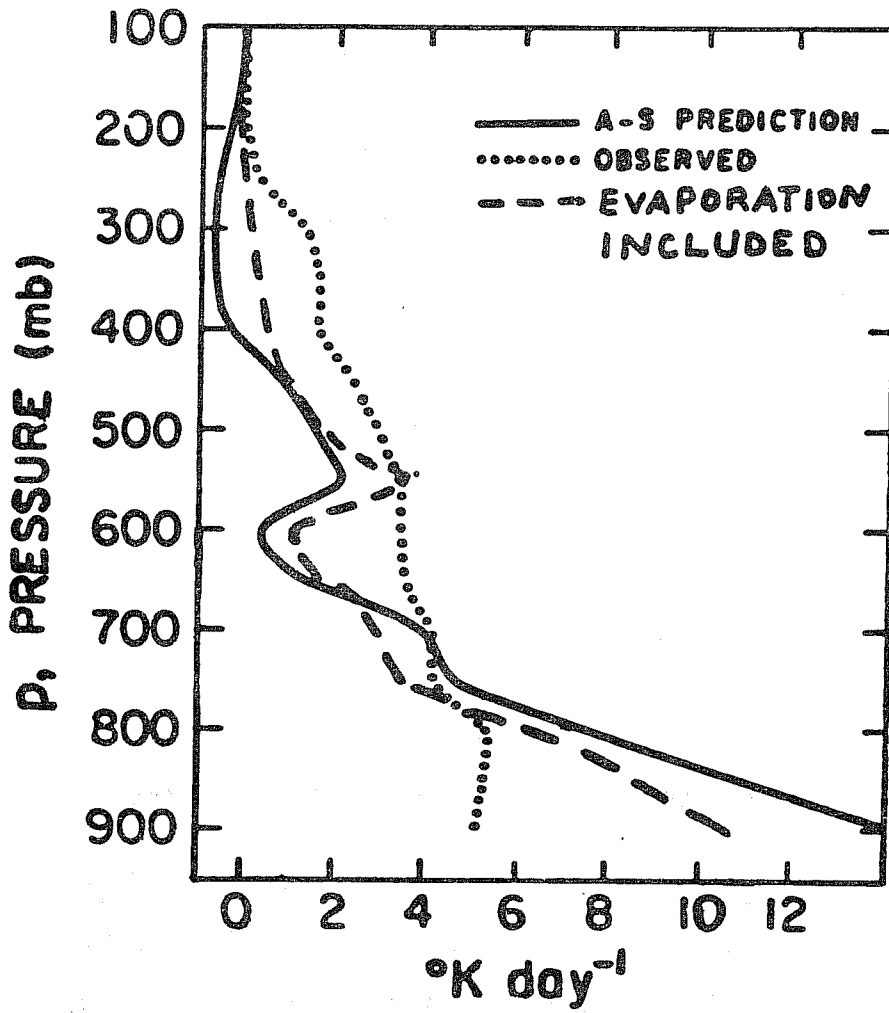
Fig. 21. Same as Fig. 19 for Q_2.

Table 1

Method		Time-Averaged Precipitation Rate (mm day^{-1})
P_{Q2}		14.3
P_{AS}		12.1
P_{KUO}		6.63
P_{MCA}	60%	11.86
$(R_H)_c$	70%	11.40
	80%	7.75
	90%	2.63

Table 2

Correlation Coefficients for Precipitation Rates

	P_{AS}	P_{Q2}	P_{RA}	P_{MCA}	P_{KUO}
P_{AS}	1.000	0.877	0.868	0.413	0.947
P_{Q2}	0.877	1.000	0.817	0.429	0.901
P_{RA}	0.868	0.817	1.000	0.472	0.850
P_{MCA}	0.413	0.429	0.472	1.000	0.435
P_{KUO}	0.947	0.901	0.850	0.435	1.000

Table 3

Predicted Time-Averaged

Cumulus Warming

$$[\frac{\partial \overline{T}}{\partial t}]_{CU}$$

$$(^{\circ}C\ day^{-1})$$

P	KUO	Moist Conv. Adj.
100	0.0	0.0
150	1.02	0.0
200	2.22	0.0
250	2.59	0.0
300	2.65	0.0
350	2.67	.17
400	2.53	10.89
450	2.39	3.30
500	2.36	1.60
550	2.31	16.03
600	2.38	1.45
650	2.11	16.97
700	1.89	.21
750	1.63	.98
800	1.48	1.65
850	1.24	2.10

Table 4

Predicted Time-Averaged

Cumulus Drying

$$- \frac{L}{c_p} [\frac{\partial \overline{q_v}}{\partial t}]_{CU}$$

$$(^\circ C \ day)$$

P	KUO	Moist Conv. Adj.
100	0.0	0.0
150	-0.02	0.0
200	-0.11	0.0
250	-0.2	0.0
300	.33	0.0
350	.04	0.13
400	-0.67	-3.90
450	-0.46	3.41
500	-0.18	3.36
550	-0.2	-7.88
600	-0.17	5.91
650	-0.31	-11.31
700	0.01	8.85
750	0.07	9.72
800	1.73	11.00
850	2.03	10.97